Texas A&M University
J. Mike Walker'66 Department of Mechanical Engineering
Turbomachinery Laboratory
Tribology Group

LEAKAGE AND ROTORDYNAMIC FORCE COEFFICIENTS OF A POCKET DAMPER SEAL AND LABYRINTH SEAL OPERATING WITH WET GAS

Annual Progress Report to the TAMU Turbomachinery Research Consortium

TRC-SEAL-01-22

Follow up to TRC-SEAL-01-21

by

José Torres
Graduate Research Assistant

Luis San Andrés
Mast-Childs Chair Professor
Principal Investigator

June 2022

WET SEALS FOR SUB-SEA MULTIPLE PHASE COMPRESSORS
TRC Project funded in 2019-2020
TEES #28-258124-00131

ABSTRACT

Centrifugal compressors utilize annular clearance gas seals to restrict excessive leakage from high-pressure regions to low-pressure regions. The pocket damper seal (PDS) and the labyrinth seal (LS) are two examples of seals commonly used in turbomachinery. Technological developments in the oil and gas industry require centrifugal compressors to operate in increasingly harsh environmental conditions. Land-based natural gas processing facilities often implement liquid and gas separators prior to compression. Such equipment is difficult to install and maintain in subsea environments. Thus, centrifugal compressors that can withstand deep sea mixtures with a liquid volume fraction (LVF) up to 5% are in high demand for offshore production facilities.

This work details experimental results for the leakage and rotordynamic performance of a PDS and a LS operating with a *wet* gas mixture made of oil and air. The two seals have similar geometry and operate with shaft speed up to 5,250 rpm (surface speed = 35 m/s) and a pressure ratio (inlet/exit) equal to 2.5. Both seals feature a journal diameter D = 127 mm and an axial length L = 48 mm. The LS has a 17% larger radial clearance ($C_{r,LS}$ = 0.230 mm, $C_{r,PDS}$ = 0.230 mm) due to a manufacturing error and limited budget to procure a new seal.

For operation with pure gas, the LS leaks more as a result of its slightly larger clearance. The loss coefficient (c_d) is a non-dimensional parameter characterizing a seal's effectiveness to reduce leakage while accounting for seal geometry. $c_d << 1$ indicates a more effective seal. The c_d of both seals is nearly identical for operation with pure gas, with the difference between the two often less than the experimental uncertainty. For operation with *wet* gas, the PDS c_d decreases as the LVF increases whereas the LS c_d increases, thus indicating the PDS is more effective to restrict *wet* gas leakage. The leakage and c_d of both seals appear impervious to an increase in shaft speed (up to 5,250 rpm).

When operating with pure gas, the direct stiffness (K) and effective damping (C_{eff}) of both seals are small in magnitude (K < 0.5 MN/m, C_{eff} < 2 kN-s/m) and often lesser than the experimental uncertainty. For operation with *wet* gas and without shaft rotation, the PDS produces a larger C_{eff}, particularly for excitation frequencies below 50 Hz. However, when operating with shaft speed equal to 3,000 and 5,250 rpm, the PDS produces a negative C_{eff} for whirl frequencies below 50 Hz. Meanwhile, the LS C_{eff} remains positive and small in magnitude for the two cases of shaft speed. The experimental results are similar for operation with LVF equal to 3% and 5%.

Unexpected low frequency motions appear when supplying the PDS with a *wet* gas. Although small in amplitude (< 5 μm), the motions appear to increase in severity as the mixture inlet LVF and shaft speed increases. The motions are entirely absent for the LS. Experiments in which *wet* gas mixture is bled directly from the cavities of the PDS rule out the possibility of liquid accumulation being the cause of the observed motions.

The experimental results presented in this work serve as a reference to turbomachinery design engineers and aid in the validation of analytical tools.

NOMENCLATURE

A	Seal Clearance Cross-Sectional Area [m^2]
c_d	Loss Coefficient [-]
C_e	Effective Clearance [m]
C_{eff}	Effective Damping [N-s/m]
$C_{ij} = C_{xx}, C_{yy}$	Direct Damping ($i = j$) [N-s/m]
$C_{ij} = C_{xy}, C_{xy}$	Cross-coupled Damping ($i \neq j$) [N-s/m]
C_r	Seal Radial Clearance [m]
d	Pocket/Cavity Depth [m]
D	Journal Diameter, $D = 2R$ [m]
f_o	Amplitude of Applied Periodic Excitation [N]
f_x	Recorded Excitation Force Along the X-Axis [N]
f_y	Recorded Excitation Force Along the Y-Axis [N]
G	Amplitude of Flexibility Function [m/N]
$H_{ij} = H_{xx}, H_{yy}$	Direct Complex Dynamic Stiffness ($i = j$) [N/m]
$H_{ij} = H_{xy}, H_{xy}$	Cross-coupled Complex Dynamic Stiffness ($i \neq j$) [N/m]
$K_{ij} = K_{xx}, K_{yy}$	Direct Stiffness ($i = j$) [N/m]
$K_{ij} = K_{xy}, K_{xy}$	Cross-coupled Stiffness ($i \neq j$) [N/m]
L	Seal Axial Length [m]
$\dot{m}$	Mass Flow Rate [kg/s]
M_{sc}	Mass of Test Rig Seal Cartridge, $M_{sc} = 14$ [kg]
P	Mixture Pressure [Pa]
PR	Seal Pressure Ratio (inlet/exit), $PR = P_s/P_e$ [-]
Q	Volumetric Flow Rate [m^3/s]
R	Journal Radius, $R = 0.5D$ [m]
R_g	Specific Gas Constant of Air [J/kg-K]
t	Elapsed Time [s]
T	Mixture Temperature [K]
U	Shaft Surface Speed, $U = \pi D\Omega/60$ [m/s]
v	Mixture Flow Velocity [m/s]
$V_{balloon}$	Total Volume of Balloons (Liquid Accumulation Experiments) [m^3]
V_{liquid}	Liquid Volume of Balloons (Liquid Accumulation Experiments) [m^3]
x, y	Seal Displacement with Respect to Shaft Along X and Y Directions [m]
$\dot{x}, \dot{y}$	Seal Velocity Along X and Y Directions [m/s]
$\ddot{x}, \ddot{y}$	Seal Absolute Acceleration Along X and Y Directions [m/s^2]
ρ	Density [kg/m^3]
$\emptyset$	Phase Angle of Flexibility Function [rad]

ω	Excitation Frequency [rad/s]
Ω	Shaft Speed, $\Omega = 60 \cdot U/\pi D$ [rpm]

Matrices and Vectors

$\mathbf{D}$	Recorded Seal Displacement in Time Domain
$\mathbf{A}$	Recorded Seal Acceleration in Time Domain
$\mathbf{F}$	Dynamic Load Applied to Seal in Time Domain
$\bar{\mathbf{D}}$	Discrete Fourier Transform of **D**
$\bar{\mathbf{A}}$	Discrete Fourier Transform of **A**
$\bar{\mathbf{F}}$	Discrete Fourier Transform of **F**
$\mathbf{H}$	Complex Dynamic Stiffness

Abbreviations

DFT	Discrete Fourier Transform
GMF	Gas Mass Fraction, GMF = 1 – LMF
GVF	Gas Volume Fraction, GVF = 1 - LVF
LMF	Liquid Mass Fraction, LMF = 1 – GMF
LVF	Liquid Volume Fraction, LVF = 1 – GVF
TOS	Teeth-On-Stator Labyrinth Seal

Subscripts

a	Axial Component of Flow Velocity
air	Air (gas)
e	Seal Exit
h	Test Rig Structure Force Coefficients
ideal	Idealized Inviscid Flow
m	Mixture (Liquid and Gas)
oil	Oil (liquid)
s	Seal Supply/inlet
seal	Seal Contribution to System Complex Dynamic Stiffness
structure	Structure Contribution to System Complex Dynamic Stiffness

TABLE OF CONTENTS

LIST OF FIGURES

LIST OF TABLES

1. INTRODUCTION

Centrifugal compressors utilize annular clearance gas seals to reduce excessive leakage of the process fluid from high-pressure regions to low-pressure regions. Examples of such seals include interstage seals, impeller eye seals, and balance-piston seals [1]. The pocket damper seal (PDS) is a type of gas seal that arose from slight modifications to the conventional labyrinth seal [2]. Unlike a labyrinth seal (LS), which consists of circumferential blades that create 360˚ cavities, a PDS includes partition walls that divide each cavity into separate "pockets".

Designers have successfully used PDSs to replace LSs in order to remedy rotordynamic stability issues as PDSs have the ability to increase their effective damping [1]. Further technological developments, particularly in the oil and gas industry, call for liquid tolerant centrifugal compressors. The presence of liquid in a gas seal, even if in miniscule amounts, can have a large impact on the rotordynamic stability and leakage characteristics of turbomachinery [3]. Currently, there is a need to quantify the rotordynamic behavior of *wet* gas seals, as experimental data is still scarce, particularly for PDSs.

This work aims to characterize the dynamic stability and leakage properties of a PDS under *wet* gas conditions, and benchmark the results against a similarly dimensioned LS. The results will help turbomachinery design engineers in selecting a seal type that best meets their system requirements and aid in the validation of current and future predictive tools.

2. LITERATURE REVIEW

Annular seals in turbomachinery are designed to restrict process gas leakage between a rotor and stator. There exists a variety of seals to choose from when designing turbomachinery, including (but not limited to) labyrinth seals (LS), honeycomb seals, hole-pattern seals, brush seals, and pocket damper seals (PDS). This literature review will focus on the experimental leakage and rotordynamic performance evaluation of PDSs operating with both pure gas and wet gas conditions. A review of computational works to predict the performance of dry and wet gas seals follows, namely bulk flow models (BFM) and computation fluid dynamics (CFD) efforts.

Experimental Leakage and Rotordynamic Performance of *Dry* Seals

Labyrinth seals (LS) often cause rotordynamic stability issues in compressors and turbines [1]. Prior experimentation shows that cross-coupled stiffness effects may be significant in LSs, which may in fact lead to rotordynamic instability [1]. These cross-coupled effects are in large part due to the development of a large circumferential velocity of the process fluid within the cavities [1]. Therefore, seals experiencing a higher degree of pre-rotated flow may have an increased susceptibility to instability issues. Another cause of fluid rotation within LS cavities is simply the shearing forces developed by the shaft surface. A design engineer may implement various modifications to remedy rotordynamic instability issues including the addition of swirl brakes, shunt holes, or replacing the seal with an improved design [1].

In 1993, Vance and Schultz [2] invented the TAMSEAL®, a first PDS derived from a conventional LS. The TAMSEAL® differs from the typical LS with two unique features. First, the seal clearance diverges along the axial flow path. In the TAMSEAL®, the clearance at the seal exit blade is twice as large as the clearance at the upstream inlet blade. The second feature is the introduction of partition walls along the circumferential direction, effectively dividing the cavity

into four identical pockets. Prior testing by Vance and Li [3] shows the TAMSEAL® successfully reduces rotor vibrations, while crossing a critical speed, by as much as 50% when compared to the effect of a similarly dimensioned conventional LS. In addition, the TAMSEAL® successfully decreases the overall synchronous response to an imbalance for operation with supply pressure up to 3.4 bar and rotor speed up to 6000 rpm (surface speed = 32 m/s). Rap tests show the novel seal design dissipates motion much quicker, indicating a much higher effective damping. As the inlet pressure of the TAMSEAL® increases, the logarithmic decrement rapidly increases. The authors illustrate how this damping is a result of the dynamic pressure variations within the PDS pockets that tend to oppose the rotor whirl motion. A caveat to the superior rotordynamic performance of the TAMSEAL® is the higher rate of leakage when compared to the conventional LS. The authors note the leakage rate of the TAMSEAL® to be approximately 30% larger than that of the LS [3].

In 1995, Richards et al. [4] present two case studies in which a PDS successfully solved instability issues in centrifugal compressors, illustrating the usefulness of using PDSs in industrial turbomachinery for dry gas applications. The first case study involves three identical trains of back-to-back low-pressure compressors (LPC) and high-pressure compressors (HPC). The authors note that although the rated operating speed of the compressors was 11,000 rpm, the LPC could only achieve 7,500 rpm, whereas the HPC could only achieve 10,600 rpm due to excessive subsynchronous vibrations (SSV) at the center LS. The LPC and HPC experienced SSVs at a frequency equal to the first natural frequency of their respective rotors. The authors believe the initial design analysis severely underestimated the magnitude of the cross-coupled stiffness contribution of the center LS. The operators initially intended to replace the center LS with a honeycomb seal to improve vibration damping, alas were unable due to the long manufacturing lead time. Instead, the operators implemented a PDS with pocket depths specifically designed to

optimize damping at the rotor natural frequency. The new configuration completely eliminated the SSV [4].

The second case study in Ref. [4] involves a set of four six-stage compressors in an offshore platform in the North Sea. These compressors were rendered inoperable due to an excessive subsynchronous vibration. The authors describe severe LS rubs at the center balance piston occurring on multiple occasions. Due to the susceptibility to rubbing and wear, the operators designed a replacement PDS made from polyamide-imide copolymer. The choice of material is based on chemical compatibility with the service conditions and excellent wear properties to prevent damage to the rotor. The results show the PDS reducing SSV amplitudes by as much as 50% at an operating speed of 11,000 rpm, while the improved material allows for operation with tighter clearances due to the reduced concern of damage occurring during a transient seal rubbing event [4].

In 1999, Ransom et al. [5] present additional early experimentation regarding the performance of PDSs. The authors corroborate the results of Vance and Li [3] by identifying the rotordynamic force coefficients of a short (L/D = 0.32) LS before and after adding radial baffles, effectively changing the configuration to that of a PDS. Their results show the presence of radial baffles change the direct damping coefficients from negative to positive while also reversing the direct stiffness from positive to negative for operation with pressure ratio (inlet/exit) ranging from 1 to 3 and a journal speed equal to 0, 1.5, and 3 krpm (rotor surface speed = 0, 10, 20 m/s). The large direct damping coefficients are significant enough to have a noticeable effect on the logarithmic decrement of the test system. The cross-coupled effects of both seals, however, are small and well within the experimental uncertainty. The authors report a nearly identical leakage performance between the two configurations, different than the results of Vance and Li [3].

When evaluating alternative designs to replace a LS causing instability issues, designers have several options to consider. In addition to PDSs, honeycomb seals and hole pattern seals also have the ability to produce favorable rotordynamic characteristics compared to a LS. In 2000, Li et al. [6] present early experimental results comparing the performance of a PDS against that of a honeycomb seal. The authors investigate the effect of inlet pre-swirl and seal eccentricity on the performance of both seals. Both seals feature identical diameter, axial length (L/D = 0.54), and radial clearance (0.254 mm). A series of rotor speed coastdown tests show the honeycomb seal has a higher effective damping than the PDS. However, the honeycomb seal produces a large positive direct stiffness that could affect the rotor critical speed. In contrast to these results, the PDS shows a negative direct stiffness (similar to a LS), indicating that the rotor critical speed may not be greatly affected if replacing a LS with a PDS. Thus, the authors argue the PDS is more suitable to serve as a drop-in-replacement for a conventional LS [6].

A PDS may feature inactive cavities between partitioned cavities (pockets). An inactive cavity is one without partition walls, thus not blocking the development of circumferential flow, similar to the conventional LS. In 2002, Li et al. [7] investigate the rotordynamic effects of having slots machined into the blades of a PDS (L/D = 0.54) with five damper cavities and four inactive cavities, thus allowing for a small amount of unobstructed axial flow. Measurements of an unbalance response reveal the slotted PDS resulted in an increase in rotor critical speed, indicating a positive direct stiffness. Recall prior results [5] show a PDS without slots changing the direct stiffness from positive to negative compared to a LS. The results also illustrate the effectiveness of the slotted PDS in reducing vibration amplitude when compared to a conventional PDS, indicating a higher effective damping. The authors show that a positive gas preswirl, defined as being of the same direction as the shaft rotation, quickly degrades the effective damping [7].

A need to characterize the performance of a PDS under operating conditions that exist in high-pressure industrial centrifugal compressors prompted Ertas and Vance [8] (2006) to use a modified high-pressure test rig originally used with hydrostatic bearings. The test facility supports experiments with rotor speeds ranging from 10,200 to 20,200 rpm (surface speed ranging from 61 to 121 m/s) and seals operating with a supply pressure up to 68.9 bar and a pressure ratio (inlet/exit) equal to 1.85. The authors illustrate the effects of clearance ratio (inlet/exit), rotor speed, and excitation frequency on the rotordynamic force coefficients of a 12-blade PDS and an 8-blade PDS. While rotor speed has a negligible effect on direct damping, clearance ratio and excitation frequency create a noticeable difference. The authors show that an increasing clearance ratio increases two-fold the direct damping. Additionally, the results illustrate that the direct damping decreases with excitation frequency; different from the behavior exhibited by most honeycomb seals and hole-pattern seals [8].

Besides rotordynamic stability, leakage is most important when selecting gas seals for use in turbomachinery. In 2011, Sheng et al. [9] compare the leakage of a LS, two fully partitioned PDSs, and a honeycomb seal. The four seal types feature an identical inner diameter of 170 mm and a radial clearance of 0.29 mm. The PDSs differ only in cavity depth, while both feature seven circumferential cavities, each divided into eight pockets. The authors estimate an effective clearance as a way to normalize the performance of each seal with respect to the properties of the process fluid and the geometry of the seal entrance. For an inlet pressure up to 20 bar and pressure ratio (inlet/exit) ranging from 1 to 2, the authors discover the honeycomb seal consistently leaks the least. The honeycomb seal provides a reduction in effective clearance of about 4% in comparison to that of the LS. On the other hand, the PDS provides an increase in effective clearance of up to 21% at the lowest inlet pressure. Thus, it is important for turbomachinery design

engineers to be aware of the higher leakage of a PDS when deciding to incorporate one into their design. Additionally, the authors illustrate that for a fixed inlet pressure, increasing the pressure ratio (inlet/exit) above 1.8~2.0 does not cause a further increase in leakage. The seal leakage reaches a limit as the flow becomes choked for pressure ratios greater than 1.8, therefore further decreasing the seal exit pressure will not cause the leakage to increase [9].

In 2020, Delgado et al. [10] present more recent experimentally derived rotordynamic force coefficients for a fully partitioned PDS operating with similar speed and pressure as those in industrial multiple-stage compressors, namely a supply pressure up to 70 bar(a) and shaft speed equal to 10, 15, and 20 krpm (surface speed = 60, 90, and 120 m/s). The test PDS features an inner diameter of 114.3 mm (L/D=0.75), a radial clearance of 0.203 mm, with seven active cavities each containing eight pockets. The authors demonstrate that the PDS direct stiffness is small in magnitude (<2 MN/m) and tends to decrease as the pressure ratio (exit/inlet) increases, thus one would expect a PDS to have a miniscule impact on the system critical speed. In addition, the experimental results agree with those presented by Li et al. [6], showing that at low frequencies the PDS direct stiffness coefficients are negative, though small in magnitude. The effective damping coefficient of the PDS increases with an increase in shaft speed and a reduction in inlet pre-swirl flow. The cross-over frequency of a seal, defined as the frequency at which the effective damping turns from negative to positive, is of great importance to turbomachinery designers. When compared to a similarly dimensioned honeycomb seal, the authors reveal that the PDS has a favorable (lower) cross-over frequency at low pre-swirl conditions, while the honeycomb seal features a favorable cross-over frequency at increased inlet pre-swirl conditions. The authors also report the PDS leaks 20%-25% more than the similarly dimensioned honeycomb seal, thus corroborating prior experimental efforts by Sheng et al. [9].

In 2021, Yang et al. [11] introduce a novel stepped shaft PDS. The new design features a conventional four-blade PDS paired with a shaft containing two unique "steps" aligned with the first and third blades of the PDS. The PDS features a radial clearance at the "step" locations equal to 0.094 mm, while the nominal radial clearance equals 0.184 mm. The steps, creating a reduced clearance at these locations, ensure a leakage reduction. The authors present experimentally derived and CFD predicted leakage and force coefficients for the novel design and an identical smooth journal PDS. The results indicate the direct dynamic stiffness turns negative when switching from a smooth to stepped journal. More importantly, the authors illustrate the superior damping performance of the stepped shaft PDS, whose effective damping is nearly 1.5 times larger than that of a uniform clearance PDS at an excitation frequency of 20 Hz.

Experimental Leakage and Rotordynamic Performance of *Wet* Seals

Technological developments in the oil and gas industry call for centrifugal compressors to operate in increasingly harsh environmental conditions. For on-land natural gas processing, separators installed upstream of a compressor inlet serve to separate gas and liquid streams prior to compression [12]. These devices are costly to install and maintain in subsea environments. Thus, centrifugal compressors that can directly withstand a wet gas mixture are in high demand in the oil and gas industry. Flow mixtures with a liquid volume fraction (LVF) up to 5% are not uncommon in offshore production facilities [13]. *Wet* gas compression technology opens up the opportunity to make efficient use of deep-sea natural gas fields.

In 2005, Brenne et al. [12] investigate the effects of a *wet* gas mixture on a single-stage centrifugal compressor originally designed for operation with pure gas. The thermodynamic performance of the *wet* gas centrifugal compressor is well understood. For example, the specific power consumption of the compressor decreases as the LVF increases from 0 to 3%, primarily due

to the higher density of the mixture increasing the overall flow rate. Nonetheless, the specific power consumption remains greater than separating liquid and gas streams prior to compression. In addition, for an inlet LVF ranging from 0 to 3%, the results indicate the pressure and temperature ratios (inlet/discharge) increase as the LVF increases. The rotordynamic behavior, however, is less conclusive. Brenne et al. illustrate that the noise and vibration levels are not greatly affected for a mixture ranging from 0 to 2% LVF. However, when LVF is equal to 3%, the experimental single-stage compressor produced a subsynchronous vibration at the drive end of the compressor shaft with a peak occurring at half the running speed. While the authors believe the rotor instability is related the liquid phase being entrained in the impeller eye and balance piston seals, the results are not conclusive [12].

In response to a demand for a more comprehensive look into the effects of wet gas compression on the mechanical performance of centrifugal compressors, Ransom et al. [14] (2011) investigate the radial and axial vibrations and shaft torque of a two-stage centrifugal compressor subjected to operation with a wet gas. For a suction pressure of 20 bar(a) and a LVF up to 5%, the results produce a negligible impact on the radial vibrations of the compressor, while axial vibrations increase significantly at a low frequency range of 10-15 Hz as the LVF increases. The authors initially theorize the increase in axial vibration is a result of inlet liquid slugging, but quickly disprove this theory by repositioning the injection flange location, and observing identical results. No further explanation for the subsynchronous vibration is provided. Furthermore, the axial thrust of the compressor decreases initially as the LVF increases from 0% to 0.5%, and then increases significantly as the LVF increases to 5%. The test compressor features significantly worn impeller eye seals with a clearance twice as large as the nominal design clearance, thus the

rotordynamic impact of a wet gas on the seals may not be representative of industrial machinery with tighter clearance seals [14].

In 2014, Vannini et al. [15] conduct a more in-depth investigation into the rotordynamic effects of wet gas ingestion into a single stage centrifugal compressor. The authors show the centrifugal compressor is able to withstand large amounts of liquid phase, noting that the synchronous vibration level only exhibits slight increases and the critical speed position is not affected. Unlike the results of Ransom et al. [14] showing a negligible impact to radial vibrations, Vannini et al. [15] report an unexpected radial subsynchronous vibrations (SSV) occurring at high flow rate and high liquid to gas density ratios. The SSV appears at a frequency equal to 45% of shaft speed with an amplitude of nearly twice the amplitude of synchronous vibration. A thorough investigation reveals the SSV is closely related to the pressure drop across the balance piston seal, leading the authors to believe the likely cause is liquid accumulation in the LS cavities. Replacing the LS with a fully partitioned pocket damper seal (FPPDS) causes a near complete elimination of the SSV. To further investigate this self-exciting phenomenon, Vannini et al. [16] (2016) perform an extensive CFD analysis of a LS and PDS operating under a wet gas condition. The analysis corroborates their earlier experimental observations, illustrating that a teeth-on-stator (TOS) LS is particularly susceptible to liquid entrapment within the cavities.

Various experimental programs aim to isolate and identify the leakage and rotordynamic behavior of annular seals operating with a two-phase mixture. San Andrés and Lu [17-19] present the leakage and rotordynamic force coefficients of short length (L/D=0.38) seals operating with air and oil mixtures, namely a smooth surface seal, a deep-grooved pattern seal, two stepped clearance seals, and a three-wave seal. The experiments aim to characterize seals for application to centrifugal pumps. Therefore, the two-phase flow is comprised of mostly liquid, producing a

bubbly mixture. For operation with a journal speed equal to 3.5 krpm (23.3 m/s) and a pressure ratio (inlet/exit) equal to 2.5, the addition of gas to a predominantly liquid mixture produces a hardening effect that increases the direct stiffness of all test seals. For operation with pure liquid, the force coefficients of each seal tend to be frequency independent. As the GVF increases (liquid phase is reduced), the force coefficients begin to vary with frequency, particularly the direct and cross-coupled stiffnesses. The direct damping of each seal increases as the GVF increases, with the three-wave seal producing the greatest amount of damping [19].

In a similar test program, Childs and students [20-22] study the static and dynamic characteristics of long annular seals (L/D=0.65-0.75) operating with a two-phase, mainly air, mixture for application to wet gas centrifugal compressors. Their test seals include a smooth annular seal, a labyrinth seal, and a honeycomb seal. The tests utilize a mixture of air and silicone oil (PSF-5cSt) with a LVF ranging from 0% to 10% and a pressure ratio (exit/inlet) ranging from 0.25 to 0.57 (inlet pressure = 62.1 bar(a)). Similar to the work by San Andrés et al. [17-19], the results show the direct and cross-coupled stiffness are frequency-dependent for all seals. The direct damping of the seals increases significantly with an increasing LVF, although the rate of increase drops as LVF increases. The honeycomb seal produces the greatest amount of direct damping, followed by the smooth seal, with the labyrinth seal producing the least. Note that the smooth surface seal and labyrinth seal produce frequency-independent direct damping, whereas the honeycomb seal produces a frequency-dependent direct damping that tends to decrease as the excitation frequency increases from 10 to 200 Hz. Nonetheless, the honeycomb seal also features the largest effective damping where the cross-over frequency decreases as the LVF increases [22].

Realizing a continued need for experimental data to validate and benchmark the numerical tools currently under development, Voigt et al. [23] (2017) introduce the design of a test facility

enabling high-precision, rotordynamic force coefficient estimation of *wet* gas seals. The test facility features a shaft supported on two active magnetic bearings. A calibration apparatus surrounding the shaft and featuring four equally spaced pneumatic pistons to apply a load to the shaft calibrates the measurement system to enable quantification of the forces generated from disturbing the seal flow. Active magnetic bearings are especially well-suited to provide the necessary perturbations. The unique test facility will enable the characterization of *wet* gas seal force coefficients with increased accuracy [23].

The aforementioned experimental programs provide plenty of insight into the effects of a two-phase mixture on the rotordynamic and leakage behavior of annular seals, including test results for a long labyrinth seal. Nonetheless, experimental rotordynamic force coefficients for a PDS operating with a *wet* gas are scarce. Yang et al. [24] (2019) provide recent experimental rotordynamic force coefficients for the operation of a fully partitioned PDS operating with a LVF equal to 0.4%. For a rotor speed equal to 5,250 rpm (35 m/s) and a pressure ratio (inlet/exit) equal to 2.3, the results indicate the direct dynamic stiffness is negative and increases as the excitation frequency is increased. Meanwhile, the direct damping is greater than the one produced under a dry gas condition [24].

The present work aims to build on the work by Yang et al. [24] and investigate the static and dynamic forced performance of a *wet* gas PDS operating with a LVF that is representative of offshore production facilities. The proposed work will vary inlet LVF from 0%-5%, while rotor surface speed varies from 0 to 35 m/s, and the pressure ratio (inlet/exit) equals 2.5. The seal to be used in the proposed work is the same design used by Yang et al. [24], hence the shaft diameter (D), axial seal length (L), inlet ($C_{r,i}$) and exit ($C_{r,e}$) clearances, number of cavities, and number of pockets is identical.

Computational Efforts to Predict Seal Leakage and Force Coefficients

A variety of computational programs exist to predict the leakage and rotordynamic force coefficients of pocket damper seals (PDSs) and labyrinth seals (LSs) operating with *dry* and *wet* gas. In 1987, Beatty and Hughes [25] present an early bulk-flow analysis to predict the leakage rate of a smooth annular seal operating with a two-phase flow. While assuming an adiabatic process and a turbulent flow through a centered seal, the authors utilize equations of mass continuity, axial and circumferential momentum transport, and energy transport. With the wall shear stresses based on empirical relations, the authors produce predictions for the leakage rate as a function of seal geometry and shaft speed. The results predict the seal leakage to decrease as the ratio of length to diameter (L/D) increases. Additionally, the leakage is expected to decrease with a sufficient increase in shaft speed or with a reduction in film thickness. The authors also demonstrate both the pressure and temperature decreases along the axial direction for an unchoked two-phase flow.

Other early efforts focus on the prediction of seal performance for operation with an ideal gas. In 1999, Li and San Andrés [26] introduce a bulk-flow predictive model for the identification of leakage and dynamic force characteristics of a multiple-pocket PDS with a single cavity. Using the assumption of an ideal and isothermal gas, the bulk-flow model includes equations of continuity, circumferential momentum, and blade tip mass flow rate conservation applied to a single control volume in a single pocket. The model includes the effects of fluid viscosity as well as flow turbulence through the use of Moody's friction factors. The authors compare the model predictions to experimental results presented by Li and Vance [27] (1995) for a PDS with a single cavity and four pockets. The model closely predicts the seal leakage obtained from the test results, with a maximum deviation of 20%, albeit producing an unusual drop in predicted leakage at a

choke pressure condition. In addition, the model results correlate well with direct damping coefficients for operation without journal speed, illustrating the direct damping increases with a greater inlet pressure [26]. In an effort to further validate the bulk-flow model, Li et al. [28] (2000) compare the model predictions with experimental results featuring a PDS with three cavities (2 active, 1 inactive), with active cavities divided into four pockets. The authors show an excellent correlation between measured and predicted seal leakage, as well as correctly predicting the leakage and force coefficients being insensitive to rotor speed [28].

In 2011, San Andrés [29] introduces a bulk-flow model for the prediction of leakage, power loss, and force coefficients of smooth and textured annular seals operating with a liquid and gas mixture. The model assumes a homogenous mixture in a thermohydrodynamic equilibrium state. The authors use the model to present predictions for a smooth annular seal with a diameter of 116.8 mm (L/D=0.75) operating with a mixture of nitrogen gas and ISO VG 2 oil at a journal speed equal to 10 krpm (61.2 m/s) and a supply pressure of 71 bar(a). The LVF of the mixture varies from 0% (pure gas) to 100% (pure liquid). Using equations of mass conservation, and axial and circumferential momentum transport, the model predicts the power loss to decrease with a decrease in LVF, with an exception occurring for LVF equal to 90%, in which power loss slightly increases before decreasing again as the LVF is reduced. The authors believe this anomaly is due to the laminarization of the flow at the mixture condition. Additionally, the model agrees with prior experimental results [17-22], showing the direct damping to increase with LVF while the direct stiffness decreases.

Also in 2011, Arghir et al. [30] introduce a bulk-flow model for predicting the rotordynamic force coefficients of textured annular seals operating with a multi-phase flow. The model assumes a homogenous mixture of liquid and gas, and considers mass conservation as well

as axial and circumferential momentum transport. Based on the Hirs assumption [31], the model assumes the wall shear stresses only depend on the local Reynolds number. The authors, recognizing that a textured seal contains a greater volume of fluid than a smooth seal, also account for a mass flow exchange between the texture cells and the mainstream flow. Using the Rayleigh-Plesset equation [32] to obtain the mixture gas volume fraction and resulting mixture properties, the authors produce predictions for a hole-pattern seal with a diameter equal to 76.5 mm (L/D = 0.46) and a clearance equal to 0.1 mm, while operating with a shaft speed of 15,500 rpm (surface speed = 62.1 m/s). With an inlet pressure equal to 57 bar(a) and an exit pressure equal to 1 bar(a), the results predict the direct stiffness to increase as the LVF decreases from 99.9% to 90%. The direct damping tends to increase as the LVF decreases from 99.9% to 90%, particularly at greater excitation frequencies. Not unexpectedly, the bulk-flow model predicts the added mass coefficients to decrease as the LVF decreases [30].

Computational fluid dynamics (CFD) analyses offer another approach to predict the leakage and rotordynamic force coefficients of dry and wet gas annular seals. In 2019, San Andrés et al. [33] present a CFD analysis to predict the leakage, drag power, and force coefficients of a smooth seal supplied with a bubbly mixture and validate against the experimental results presented in Ref. [18]. For a LVF ranging from 100% to 10% and a pressure ratio (inlet/exit) equal to 1.5, the CFD model correctly predicts the cross-coupled stiffness to decrease with a decrease in LVF, as well as the presence of the direct stiffness hardening effect previously observed in Ref. [18]. In addition, similar to the experimental results, the CFD analysis produce an effective damping of the seal to decrease as the LVF reduces. The total drag power decreases linearly with a reduction in LVF [33]. Although proven to be quite accurate, the downside of running a CFD analysis to predict

the leakage and force coefficients of annular seals is the required time compared to the much faster turnaround time of a bulk-flow model.

In 2020, Cangioli et al. [34] introduce a novel bulk-flow model for a dry gas PDS using two control volumes within each circumferential pocket. For each control volume, the model considers continuity, circumferential momentum, and energy equations. The use of two control volumes allows for the modeling of the recirculating flow within a pocket, an aspect not considered in prior work. To validate this model, the authors compare to experimental results for a fully partitioned PDS with a diameter of 0.22 m (L/D=0.30), radial clearance equal to 0.35 mm, and for operation with journal speed up to 10 krpm (surface speed = 115.2 m/s) and pressure ratio (inlet/exit) equal to 2.5. The predicted rotordynamic force coefficients, namely direct and cross-coupled stiffness, direct damping, and effective damping, show an excellent correlation with experimental measurements for positive and negative inlet pre-swirl conditions. Predicted leakage is well within the range of experimental uncertainty of the test results [34].

More recently, in 2021, Lu et al. [35] present a nonhomogenous bulk flow model (NHBFM) for annular seals operating with a gas in liquid mixture. The NHBFM considers the liquid and gas as two independent isothermal components and utilizes equations of mass conservation, and circumferential and axial momentum transport. A comparison to prior experimental results [17] reveals the NHBFM produces accurate prediction of direct stiffness, showing a quick decrease with a rise in gas content. A comparison of the direct damping coefficients reveals a deviation from experimental results of no more than 5% [35].

Also in 2021, Yang and San Andrés [36], introduce a simple analytical two-phase flow model to predict the cavity pressures and leakage of both PDSs and LSs operating with a liquid in gas mixture. The novel method adapts the well-known Neumann's Equation [37] to a two-phase

flow and uses the properties of an assumed homogenous mixture. The predictions gathered from this simple tool are compared to experimental results for a four-blade, eight-pocket PDS operating with a low pressure drop and at a low speed, and an eight-blade, sixteen-pocket PDS operating with a high pressure drop and at a high speed. For the four-blade PDS, the gas leakage predictions agree quite well with the experimental results, and with cavity pressures deviating from a CFD analysis by no more than 18%. For the eight-blade PDS, predictions for a 92% GVF mixture differ from CFD predictions by at most 6%. Besides accuracy, the greatest utility of this analytical tool is its quickness and readiness for routine engineering analyses [36].

Computational analyses of *wet* gas annular damper seals are currently an ongoing effort and in need of verification. Computational tools to predict the static and dynamic forced performance of *wet* gas PDSs are particularly limited. The simple analytical tool developed by Yang and San Andrés [36] helps remedy this issue. However, parallel experimental programs are required to validate such tools. Currently, experimental data characterizing the leakage and force coefficients of a *wet* gas PDS are scarce. The proposed work will remedy this need, helping to validate current and future analytical tools.

3. DESCRIPTION OF EXPERIMENTAL FACILITY AND TEST SEALS

Description of Test Rig

The two-phase flow (*wet* gas) test rig has a long history of providing experimentally derived seal dynamic force coefficients at Texas A&M University. San Andrés et al. [17,18,19] provide an in-depth description of the design of the wet gas test rig. Figure 1 illustrates the wet gas test rig under its current configuration. At the center of the test rig is a seal cartridge that contains the seal being tested, either a PDS or a LS. At the top of the seal cartridge lies an inlet fitting that attaches to a hose which supplies the test seal with a mixture of pressurized oil and air. Four equally spaced cylindrical rods support the seal cartridge. The structural properties (stiffness, damping, and mass) of the seal cartridge and support rods are known, allowing for the identification of the dynamic response of the test seal to external force excitations. Two orthogonally positioned electromagnetic shakers induce frequency dependent excitation forces onto the seal cartridge, thus exciting the oil and air mixture flow within the test seal.

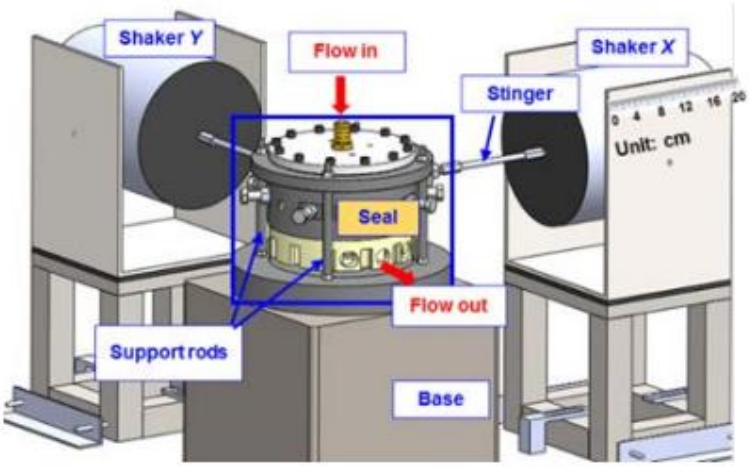

Figure 1. Test rig illustration

Figure 2 presents a cross-sectional view of the test seal cartridge. Both the stepped PDS and the stepped LS have a total length L = 0.048 m while the rotor diameter is $D = 2R$ = 0.127 m. The PDS and LS differ slightly in radial clearance due to a manufacturing error. The PDS has a radial clearance $C_{r,PDS}$ = 0.196 mm while the LS has a radial clearance $C_{r,LS}$ = 0.23 mm, i.e. 17% larger.

Four centering bolts located along the outside of the seal cartridge move and position the test seal concentric with the center of a journal. In Fig. 2, the flow of wet gas is depicted with arrows, beginning at the inlet fitting and ending at the discharge chamber. A porous metal mixing sparger with pore size of 2 μm directly upstream of the inlet fitting mixes dry air and ISO-VG10 oil to create a liquid in gas mixture. A 0-6.9 bar(g) pressure transducer threaded into the top lid (not depicted in Fig. 3) measures the supply pressure of the wet gas prior to entering the plenum upstream of the test seal.

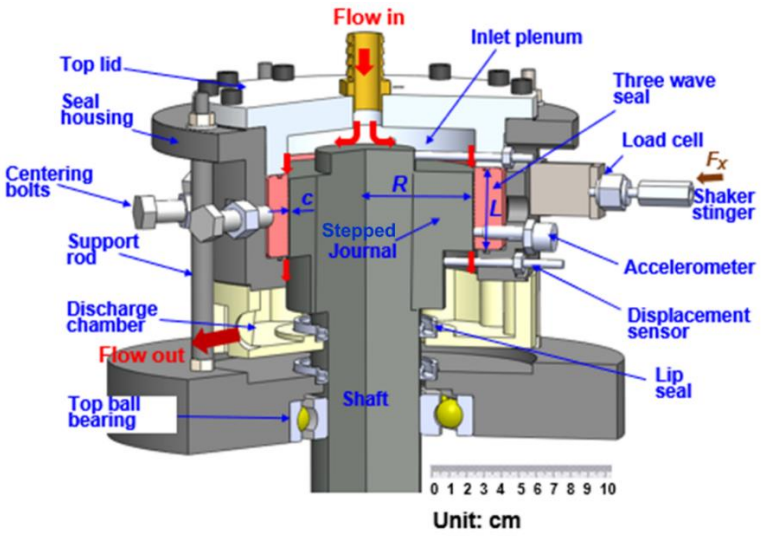

Figure 2. Cross-sectional view of seal cartridge showing mixture flow path.

Upstream of the sparger element are two separate supply lines, one for the oil and one for dry air, as depicted in Fig. 3. A supply pump draws from the oil reservoir and moves oil through the supply line. Downstream of the pump lies a flow control valve and a flow meter with a range of 0.1 to 10 gallons per minute. The control valve allows for adjustment of oil flow to achieve the desired mixture composition. Regular shop air supplies an upstream pressure of 8.3 bar(g) into the dry air supply line. The air filter/dryer system removes any contamination or moisture from the shop air. The turbine flow meter requires a pressure of 6.9 bar(g) for accurate measurement of air volumetric flow rate. Therefore, a pressure regulator is positioned directly upstream of the turbine flow meter to reduce the air pressure from 8.3 to 6.9 (bar)g. Lastly, the air flow control valve directly downstream of the turbine flow meter modulates the flow of air. When used in conjunction with the oil flow control valve, the air flow control valve allows for the adjustment of wet gas composition and supply pressure.

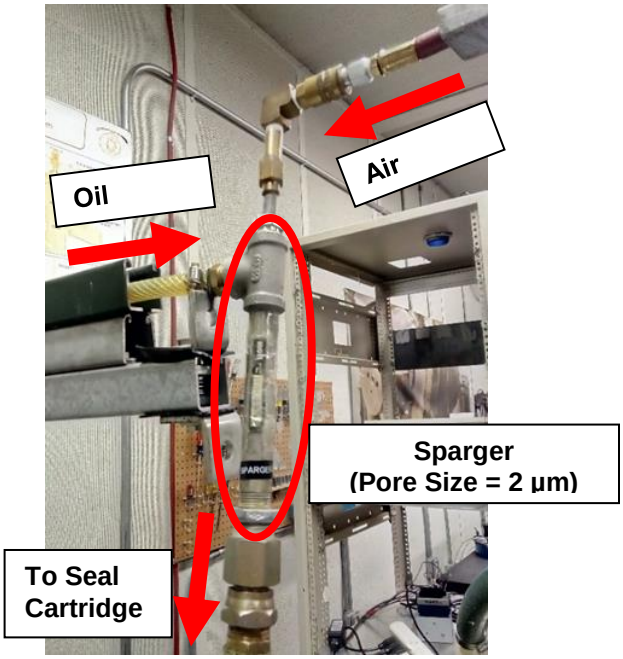

Figure 3. Sparger element with two supply lines for mixing oil and air.

The test seal cartridge hosts pairs of orthogonally placed piezoelectric accelerometers, eddy current displacement probes, and load cells. Figure 2 depicts the installation locations of the aforementioned sensors that measure the acceleration of the test seal, the displacement of the test seal with respect to the concentric journal, and the load applied to the test seal by the electromagnetic shakers, in two orthogonal directions, respectively. The manner in which the electromagnetic shakers connect to the load cells using stingers is shown in in Fig. 2. Figure 1 also shows the stingers connecting to the aforementioned electromagnetic shakers. The oil in air mixture flowing between the journal and test seal as well as the support structure produce reactions to the applied dynamic loads.

Description of Test Seals

The PDS and LS have similar dimensions to provide a vis-à-vis comparison of their performance. Table 1 presents the dimensions of both seals. Both seals have the same length *L*, journal diameter *D*, and cavity depth *d*, although featuring slightly different radial clearances C_r due to manufacturing error and a limited budget to procure a new seal. The primary differences between the two seals lie in the thickness of the blades (ribs) and the width of the cavities/pockets.

Table 1. Geometry of test seals.

Stepped Pocket Damper Seal		**Stepped Labyrinth Seal**	
Seal Length, *L*	48 ±0.03 mm	Seal Length, *L*	48 ±0.03 mm
Journal Diameter, *D*	127 ±0.013 mm	Journal Diameter, *D*	127 ±0.013 mm
*Seal Clearance, $C_{r,PDS}$	0.196 ±0.007 mm	*Seal Clearance, $C_{r,LS}$	0.230 ±0.007 mm
Pocket/Cavity Depth, *d*	4.8 ±0.03 mm	Cavity Depth, *d*	4.8 ±0.03 mm
Pocket/Cavity Width	10.5/4.8 ±0.03 mm	Cavity Width	11.6 ±0.03 mm
Rib Width	2.5 ±0.03 mm	Tip Thickness	0.2 ±0.03 mm

Figures 4 (a) and (b) present 3D models and cross-sectional diagrams illustrating the direction of flow and dimensions of the various features in the PDS and LS respectively. The PDS, made of 6061-T6 aluminum alloy, features four blades, sectioning off the seal into three rows of cavities. The center cavity has a width of 4.8 mm, whereas the other cavities are 10.5 mm wide. All PDS pockets and cavities have a depth of 4.8 mm. All blades and partition walls for the PDS are 2.5 mm in thickness. A total of eight partition walls are positioned between two adjacent blades, dividing each cavity into eight equally spaced pockets. The LS, also made of 6061-T6 aluminum alloy, consists of three equally spaced cavities with a width of 11.6 mm and a depth of 4.8 mm. Each blade of the LS is angled at 5 degrees and has a tip width of 2.5 mm.

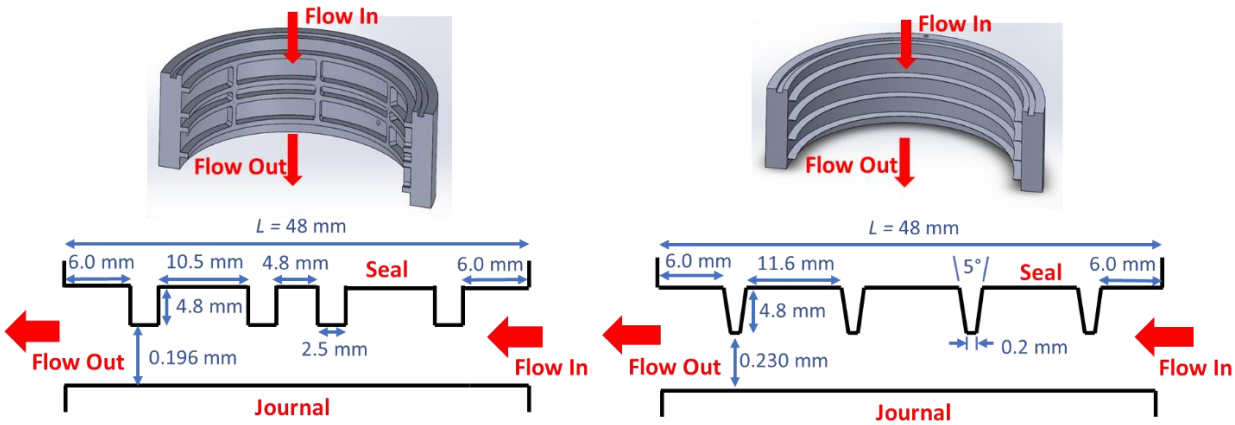

(a) Pocket Damper Seal **(b) Labyrinth Seal**

Figure 4. Cross-sectional diagrams illustrating dimensions of test (a) PDS and (b) LS (Not to scale).

4. EXPERIMENTAL PROCEDURE

Measurements of Seal Leakage

Two turbine flow meters record the liquid volumetric flow rate (Q_{oil}) and gas volumetric flow rate at the seal inlet ($Q_{air,s}$). The air flow meter displays the volumetric flow at standard conditions; hence,

$$Q_{air,s} = Q_{recorded}\left(\frac{1\,\text{bar}}{P_s}\right)\left(\frac{T_s}{289\,\text{K}}\right) \tag{1}$$

The mass flow rate of oil and air is equal to $\dot{m}_{oil} = \left(\rho_{oil}\, Q_{oil}\right)$ and $\dot{m}_{air} = \left(\rho_{air.s}\, Q_{air,s}\right)$, respectively, where $\rho_{air,s} = {P_s}/{R_g T_s}$ denotes the air density at the inlet pressure and temperature calculated using the ideal gas law. The total seal leakage is the sum of the liquid and gas mass flow rates.

$$\dot{m} = \dot{m}_{air} + \dot{m}_{oil} \tag{2}$$

Hence, the liquid mass fraction (LMF) of the mixture flowing across the seal clearance equals

$$\text{LMF} = \frac{\dot{m}_{oil}}{\dot{m}} = (1 - \text{GMF}) \tag{3}$$

The liquid volume fraction (LVF) represents the ratio of liquid volumetric flow to the total volumetric flow of the mixture and varies axially as the mixture pressure decreases. The LVF at the seal inlet (LVF_s) equals

$$\text{LVF}_s = \frac{Q_{oil}}{Q_{oil} + Q_{air,s}} = \left(1 - \text{GVF}_s\right) \tag{4}$$

where GVF_s denotes the gas volume fraction (GVF) at the seal inlet. The LVF at the seal inlet relates to the LMF by

$$\mathrm{LMF} = \frac{\mathrm{LVF}_s \cdot \rho_{air,s}}{\mathrm{LVF}_s \cdot \rho_{air,s} + (1 - \mathrm{LVF}_s) \cdot \rho_{oil}} \tag{5}$$

Measurements of seal leakage take place for a variety of operating conditions, namely pressure ratio (inlet/exit), LVF, and shaft speed. In practice, the operator first brings the rotor to the desired speed using the electric motor. The operator then opens the air flow control valve until achieving the desired pressure ratio using a pure gas flow (LVF = 0%). After recording the seal leakage, the operator slightly closes the air flow control valve, thus slightly reducing the supply pressure. The oil flow control valve is then slightly opened until once again reaching the predetermined pressure ratio. This process of closing the air flow control valve and subsequently opening the oil flow control valve serves to increase the LVF. Once measurements for the full range of LVF are complete, the operator may vary the pressure ratio or shaft speed to change the operating conditions.

This work presents the total leakage ($\dot{m}$) and a non-dimensional orifice-like loss coefficient (c_d) for each seal vs. pressure ratio (P_s/P_e) and LVF. c_d relates the actual radial clearance of the test seal (C_r) to the effective clearance (C_e) of an equivalent single-restriction seal operating with an ideal and inviscid fluid [38].

$$C_e = c_d C_r \tag{6}$$

Derived from Bernoulli's Equation, the mass flow rate through the equivalent seal is a function of the pressure drop across the seal (P_s-P_e), the average mixture density ($\bar{\rho}_m$), and the effective clearance under the single restriction ($\pi\, D\, C_e$) [38].

$$\dot{m} = (\pi D C_e)\sqrt{2\bar{\rho}_m (P_s - P_e)} \tag{7}$$

Note that for flow with just air (LVF = 0), the average mixture density is given by

$$\bar{\rho}_m = \bar{\rho}_{air} = \frac{\bar{P}_m}{R_g T_s} \tag{8}$$

where $\bar{P}_m = \frac{1}{2}(P_s - P_e)$ represents the average pressure between the seal inlet and exit. For a mixture of oil and air, the average mixture density is given by

$$\bar{\rho}_m = \overline{\mathrm{LVF}}\,\rho_{oil} + \left(1 - \overline{\mathrm{LVF}}\right)\bar{\rho}_{air} \tag{9}$$

where $\overline{\mathrm{LVF}} = \frac{1}{2}(\mathrm{LVF}_s + \mathrm{LVF}_e)$ denotes an average LVF. Note that the exit LVF is calculated as [36]:

$$\mathrm{LVF}_e = \frac{P_s \cdot \mathrm{LVF}_s}{P_s \cdot \mathrm{LVF}_s + (1 - \mathrm{LVF}_s)P_e} \tag{10}$$

Substitution of Eq. 6 into Eq. 7 gives

$$\dot{m} = c_d(\pi D C_r)\sqrt{2\bar{\rho}_m(P_s - P_e)} = c_d \dot{m}_{ideal} \tag{11}$$

Thus, c_d relates the measured mass flow rate ($\dot{m}$) to the ideal mass flow rate ($\dot{m}_{ideal}$) of a single-restriction seal with radial clearance C_r. Hence, c_d quantifies the effectiveness of a seal to reduce leakage; a lower c_d denotes a more effective seal. c_d can readily be calculated from measurements of seal leakage, seal radial clearance, and mixture pressure and density.

Rotordynamic Force Coefficients

San Andrés [39] details the procedure for identifying the dynamic force coefficients of mechanical systems. The test seal and its stator are represented as a lumped mass (M_{sc}), displacing along two degrees of freedom (x, y). Figure 5 provides a representation of the test seal with springs and dashpots denoting the stiffness (K) and damping (C) coefficients of the test seal. K_h and C_h represent the stiffness and damping of the support structure respectively.

The elastic support structure and test seal react to dynamic forces applied to the seal stator, while the spinning journal is assumed to be rigid. The response of the test seal to a dynamic load is a function of the properties of the oil and air mixture flowing between the seal and the journal and the excitation frequency. Note that K_{ij} and C_{ij} in Fig. 5 represent stiffness and damping coefficients produced by a change in force along the "*i*" direction due to a motion in the "*j*" direction.

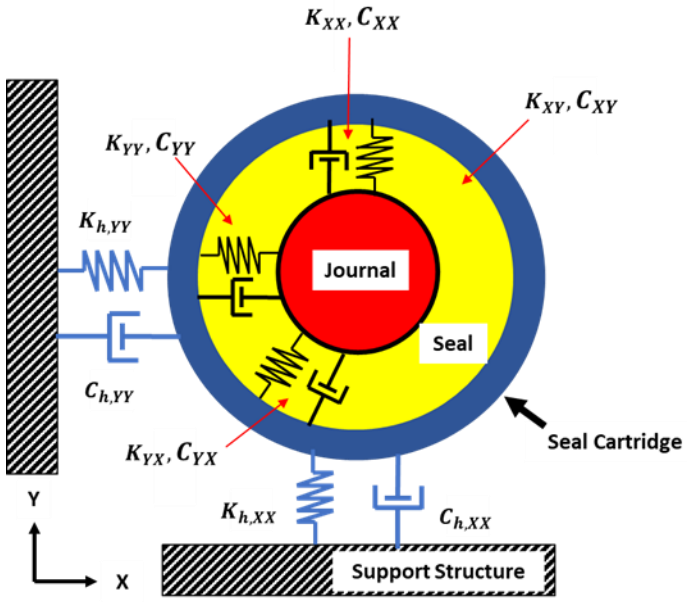

Figure 5. Representation of lumped mass with two degrees of freedom assumption used in the identification of force coefficients [39].

The equations of motion for the mechanical system described in Fig. 5 are [39]:

$$M_{sc}\ddot{x}+\left(C_{xx}+C_{h,xx}\right)\dot{x}+C_{xy}\dot{y}+\left(K_{xx}+K_{h,xx}\right)x+K_{xy}y=f_x$$

$$M_{sc}\ddot{y}+\left(C_{yy}+C_{h,yy}\right)\dot{y}+C_{yx}\dot{x}+\left(K_{yy}+K_{h,yy}\right)y+K_{yx}x=f_y \quad (12)$$

where M_{sc} = 14 kg represents the equivalent mass of the seal stator, and f_x and f_y represent dynamic force excitations applied to the stator by the electromagnetic shakers.

San Andrés [39] provides a step-by-step procedure to identify the dynamic force coefficients of the system. The first step consists of applying two separate and independent force excitations to the seal stator. These excitations are known dynamic loads exerted at a single frequency. The first excitation consists of a force entirely in the *x*-direction while the second excitation consists of a force entirely in the *y*-direction:

$$\mathbf{F_X} = \begin{bmatrix} f_{xx} = f_o e^{i\omega t} \\ 0 \end{bmatrix}, \ \mathbf{F_Y} = \begin{bmatrix} 0 \\ f_{yy} = f_o e^{i\omega t} \end{bmatrix} \tag{13}$$

where f_o and ω represent the amplitude and frequency of the applied load, respectively. Sensors record the displacement and acceleration of the seal cartridge with respect to the fixed journal and the dynamic load applied by the electromagnetic shakers at a sampling rate of 16,384 samples/s.

Let $\mathbf{D_X}$, $\mathbf{D_Y}$, $\mathbf{A_X}$, and $\mathbf{A_Y}$, denote the measured displacement and acceleration in the two orthogonal directions of the seal stator for the two sets of excitations over a set period of time:

$$\mathbf{D_X} = \begin{bmatrix} x_x \\ y_x \end{bmatrix}, \ \mathbf{D_Y} = \begin{bmatrix} x_y \\ y_y \end{bmatrix}$$

$$\mathbf{A_X} = \begin{bmatrix} \ddot{x}_x \\ \ddot{y}_x \end{bmatrix}, \ \mathbf{A_Y} = \begin{bmatrix} \ddot{x}_y \\ \ddot{y}_y \end{bmatrix} \tag{14}$$

Next, the discrete Fourier Transform of the recorded time domain data brings the data into the frequency domain. Let $\bar{\mathbf{F}}_{(\omega)}$, $\bar{\mathbf{D}}_{(\omega)}$, and $\bar{\mathbf{A}}_{(\omega)}$ denote vectors containing the amplitudes of the discrete Fourier Transform (DFT) of the measured dynamic loads, displacements, and accelerations at a specified frequency:

$$\bar{\mathbf{F}}_{\mathbf{X}(\omega)} = \mathrm{DFT}(\mathbf{F_X}) = \begin{bmatrix} \bar{F}_{xx(\omega)} \\ 0 \end{bmatrix}, \ \bar{\mathbf{F}}_{\mathbf{Y}(\omega)} = \mathrm{DFT}(\mathbf{F_Y}) = \begin{bmatrix} 0 \\ \bar{F}_{yy(\omega)} \end{bmatrix}$$

$$\bar{\mathbf{D}}_{\mathbf{X}(\omega)} = \mathrm{DFT}(\mathbf{D}_{\mathbf{X}}) = \begin{bmatrix} \bar{x}_{x(\omega)} \\ \bar{y}_{x(\omega)} \end{bmatrix},\ \bar{\mathbf{D}}_{\mathbf{Y}(\omega)} = \mathrm{DFT}(\mathbf{D}_{\mathbf{Y}}) = \begin{bmatrix} \bar{x}_{y(\omega)} \\ \bar{y}_{y(\omega)} \end{bmatrix}$$

$$\bar{\mathbf{A}}_{\mathbf{X}(\omega)} = \mathrm{DFT}(\mathbf{A}_{\mathbf{X}}) = \begin{bmatrix} \bar{a}_{xx(\omega)} \\ \bar{a}_{yx(\omega)} \end{bmatrix},\ \bar{\mathbf{A}}_{\mathbf{Y}(\omega)} = \mathrm{DFT}(\mathbf{A}_{\mathbf{Y}}) = \begin{bmatrix} \bar{a}_{xy(\omega)} \\ \bar{a}_{yy(\omega)} \end{bmatrix} \tag{15}$$

The procedure then calls for forming the following matrices:

$$\bar{\mathbf{F}}_{(\omega)} = \left[\bar{\mathbf{F}}_{\mathbf{X}(\omega)} \,|\, \bar{\mathbf{F}}_{\mathbf{Y}(\omega)}\right],\ \bar{\mathbf{D}}_{(\omega)} = \left[\bar{\mathbf{D}}_{\mathbf{X}(\omega)} \,|\, \bar{\mathbf{D}}_{\mathbf{Y}(\omega)}\right],\ \bar{\mathbf{A}}_{(\omega)} = \left[\bar{\mathbf{A}}_{\mathbf{X}(\omega)} \,|\, \bar{\mathbf{A}}_{\mathbf{Y}(\omega)}\right] \tag{16}$$

Substitution of the discrete Fourier Transform into the governing equations of motion provides the equations of motion in the frequency domain:

$$\mathbf{H}_{(\omega)}\bar{\mathbf{D}}_{(\omega)} = \bar{\mathbf{F}}_{(\omega)} - M_{sc}\bar{\mathbf{A}}_{(\omega)} \tag{17}$$

where $\mathbf{H}_{(\omega)}$ is the system complex dynamic stiffness defined as

$$\mathbf{H}_{(\omega)} = \begin{bmatrix} [(K_{xx} + K_{h,xx}) + (C_{xx} + C_{h,xx})i\omega] & [K_{xy} + C_{xy}i\omega] \\ [K_{yx} + C_{yx}i\omega] & [(K_{yy} + K_{h,yy}) + (C_{yy} + C_{h,yy})i\omega] \end{bmatrix} \tag{18}$$

Note that the complex dynamic stiffness $\mathbf{H}_{(\omega)}$ superimposes contributions from both the seal and the test rig structure:

$$\mathbf{H}_{(\omega)} = \mathbf{H}_{\mathrm{Seal}(\omega)} + \mathbf{H}_{\mathrm{Structure}(\omega)} \tag{19}$$

$\mathbf{H}_{\mathrm{Structure}(\omega)}$ is first identified from performing dynamic load tests with a dry (non-lubricated) system at ambient pressure, i.e. no pressurized mixture flowing within the seal. With $\mathbf{H}_{\mathrm{Structure}(\omega)}$ known, the components of $\mathbf{H}_{\mathrm{Seal}(\omega)}$ are readily calculated as

$$\mathbf{H}_{\mathrm{Seal}(\omega)} = [\mathbf{H}_{(\omega)} - \mathbf{H}_{\mathrm{Structure}(\omega)}] = \begin{bmatrix} H_{xx} & H_{xy} \\ H_{yx} & H_{yy} \end{bmatrix} \tag{20}$$

The components of the dynamic stiffness $\mathbf{H}_{\mathrm{Seal}(\omega)}$ are a set of complex numbers, where the real and imaginary parts correspond to the seal stiffness and damping, respectively:

$$\begin{bmatrix} H_{xx} & H_{xy} \\ H_{yx} & H_{yy} \end{bmatrix} = \begin{bmatrix} K_{xx} & K_{xy} \\ K_{yx} & K_{yy} \end{bmatrix} + i\omega \begin{bmatrix} C_{xx} & C_{xy} \\ C_{yx} & C_{yy} \end{bmatrix} \tag{21}$$

The seal element is assumed to be perfectly concentric with the rotor, thus providing identical direct stiffnesses, $H_{xx} = H_{yy} = (K + i\omega C)$, and asymmetric cross-coupled stiffness, $H_{xy} = -H_{yx} = (k + i\omega c)$. The effective damping of the seal (C_{eff}) is then calculated from the direct damping of the seal (C) as well as the cross-coupled stiffness (k).

$$C_{eff} = C - k/\omega = [\text{Ima}(H_{xx}) - \text{Real}(H_{xy})]/\omega \tag{22}$$

5. EXPERIMENTAL RESULTS AND DISCUSSION

Seal Leakage

Figure 6 presents the leakage ($\dot{m}$) and loss coefficient (c_d) of the labyrinth seal (LS) and pocket damper seal (PDS) vs. pressure ratio (P_s/P_e) for operation with pure gas and a shaft speed equal to 0, 3000, and 5250 rpm (surface speed = 0, 20, 35 m/s). Appendix A presents a detailed analysis of the experimental uncertainty for the measurement of seal leakage. Error bars in Fig. 6 depict the uncertainty for each data point. The maximum uncertainty for the measured pure gas leakage is ±1.25 g/s.

The results depicted in Figure 6 reveal a linear relationship between the recorded $\dot{m}$ for both seals and the pressure ratio across each seal. For these tests, the operator sets the pressure ratio by increasing the seal inlet pressure. As expected, the $\dot{m}$ of both seals increases as the pressure ratio increases. The LS has a larger $\dot{m}$ than the PDS due to the slightly larger clearance, $C_{r,LS}$ = 0.230 mm vs. $C_{r,PDS}$ = 0.196 mm. The $\dot{m}$ of the LS is approximately 20% larger than the $\dot{m}$ of the PDS, consistent across a pressure ratio ranging from 1.1 to 2.7 and for all shaft speed settings. Note that an increase in shaft speed produces a negligible change in leakage for both seals. The recorded leakage of the PDS and LS for operation with shaft speed deviates by no more than 2% from their respective leakage without shaft rotation. Note the mass flow rate across the seal is only dependent on the axial component of the flow velocity.

Table 2 lists the magnitudes of the exit axial and circumferential flow velocities, illustrating that even for the lowest flow condition, the axial velocity is much greater than the circumferential component. Note that the gas mean circumferential velocity is estimated as half the shaft surface

speed ($U = \pi D\Omega/60$), whereas the exit axial velocity depends on the mass flow rate and air density at the seal exit.

$$v_c = \frac{U}{2} \ , \ v_{a,e} = \frac{\dot{m}}{\rho_e \cdot \pi D C_r} \tag{23}$$

Table 2. Comparison of estimated circumferential and axial flow velocities at the seals' exit plane.

	PDS				**LS**			
	Ω = 3000 rpm		Ω = 5250 rpm		Ω = 3000 rpm		Ω = 5250 rpm	
P_s/P_e	v_c [m/s]	$v_{a,e}$ [m/s]	v_c [m/s]	$v_{a,e}$ [m/s]	v_c [m/s]	$v_{a,e}$ [m/s]	v_c [m/s]	$v_{a,e}$ [m/s]
1.14	20.0	57.6	34.9	58.2	20.0	69.2	34.9	67.6
1.28		92.6		91.0		102.4		101.6
1.41		120.7		117.4		129.0		128.2
1.55		145.0		141.0		153.9		151.0
1.69		168.3		162.0		175.9		174.2
1.83		189.1		182.3		196.7		194.6
1.97		209.0		202.3		217.4		214.1
2.10		229.4		220.9		237.8		234.4
2.24		248.8		239.5		257.3		254.8
2.38		267.8		257.6		276.4		273.9
2.52		285.7		275.6		296.3		293.0

Figure 6 also reveals the loss coefficient (c_d) of both seals is nearly constant for a pressure ratio (inlet/exit) greater than 1.5. Interestingly, the PDS and LS produce a nearly identical c_d, with the difference between the two often being less than the experimental uncertainty. For the cases when shaft speed equals 0 and 3,000 rpm; the PDS c_d is equal to approximately 0.43 whereas the LS c_d is equal to 0.44 for a pressure ratio ($PR = P_s/P_e$) greater than 1.5. For a ratio less than 1.5, both seals exhibit a slight decrease in c_d. Interestingly, when the shaft speed increases to 5,250 rpm, the c_d of both seals decreases. The c_d of the PDS and LS for operation with a pressure ratio greater than 1.5 and shaft speed equal to 5250 rpm is equal to 0.41 and 0.43, respectively. Thus, the PDS is slightly more effective than the LS in reducing pure gas leakage.

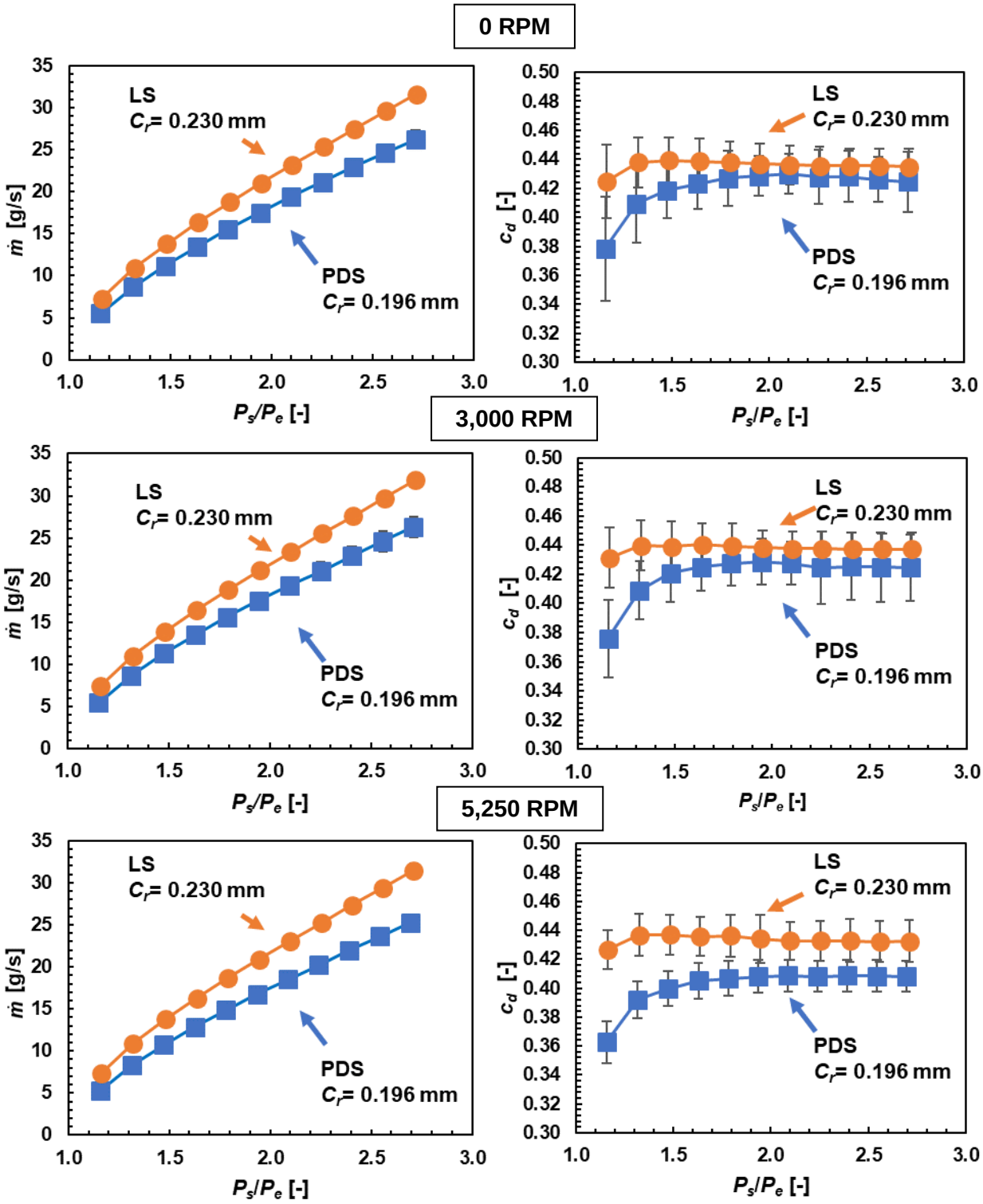

(a) Leakage, $\dot{m}$ (b) Loss Coefficient, c_d

Figure 6. PDS and LS: Leakage ($\dot{m}$) and loss coefficient (c_d) vs. pressure ratio (P_s/P_e). Operation with pure gas (LVF = 0%) and shaft speed = 0 rpm (top), 3,000 rpm (middle), and 5,250 rpm (bottom).

Figure 7 presents the *wet* gas leakage ($\dot{m}$) and loss coefficient (c_d) of the labyrinth seal (LS) and pocket damper seal (PDS) vs. inlet LVF for operation with pressure ratio (inlet/exit) equal to 2.5 and shaft speed equal to 0, 3,000, and 5,250 rpm. The results in Fig. 7 reveal a substantially larger $\dot{m}$ of the LS compared to that of the PDS. The LS leaks between 120% and 150% more than the PDS for operation with a mixture inlet LVF ranging from 3% to 5% (LMF = 89% - 94%). Recall that for operation with pure gas (Figure 6) the LS shows a $\dot{m}$ that is only approximately 20% greater than that of the PDS.

Interestingly, the c_d for both seals exhibits different behavior as the mixture inlet LVF increases. Recall the c_d of the PDS and LS for operation with pure gas and no shaft rotation equals 0.43 and 0.44, respectively. As the LVF increases, the PDS c_d initially exhibits a quick drop in magnitude, decreasing from 0.43 to approximately 0.31. Conversely, the LS c_d becomes greater in magnitude as the LVF increases, increasing from 0.44 to 0.61. After the initial increase or decrease, the c_d of both seals remains constant as the mixture LVF further increases. Recall that a lower c_d indicates a more effective seal in reducing leakage. Thus, for operation without shaft rotation, the results illustrate the PDS is a more effective seal in reducing *wet* gas leakage than the LS. Note that the *wet* gas $\dot{m}$ and c_d both appear to be impervious to the increase in shaft speed from 0 rpm to 3,000 and 5,250 rpm.

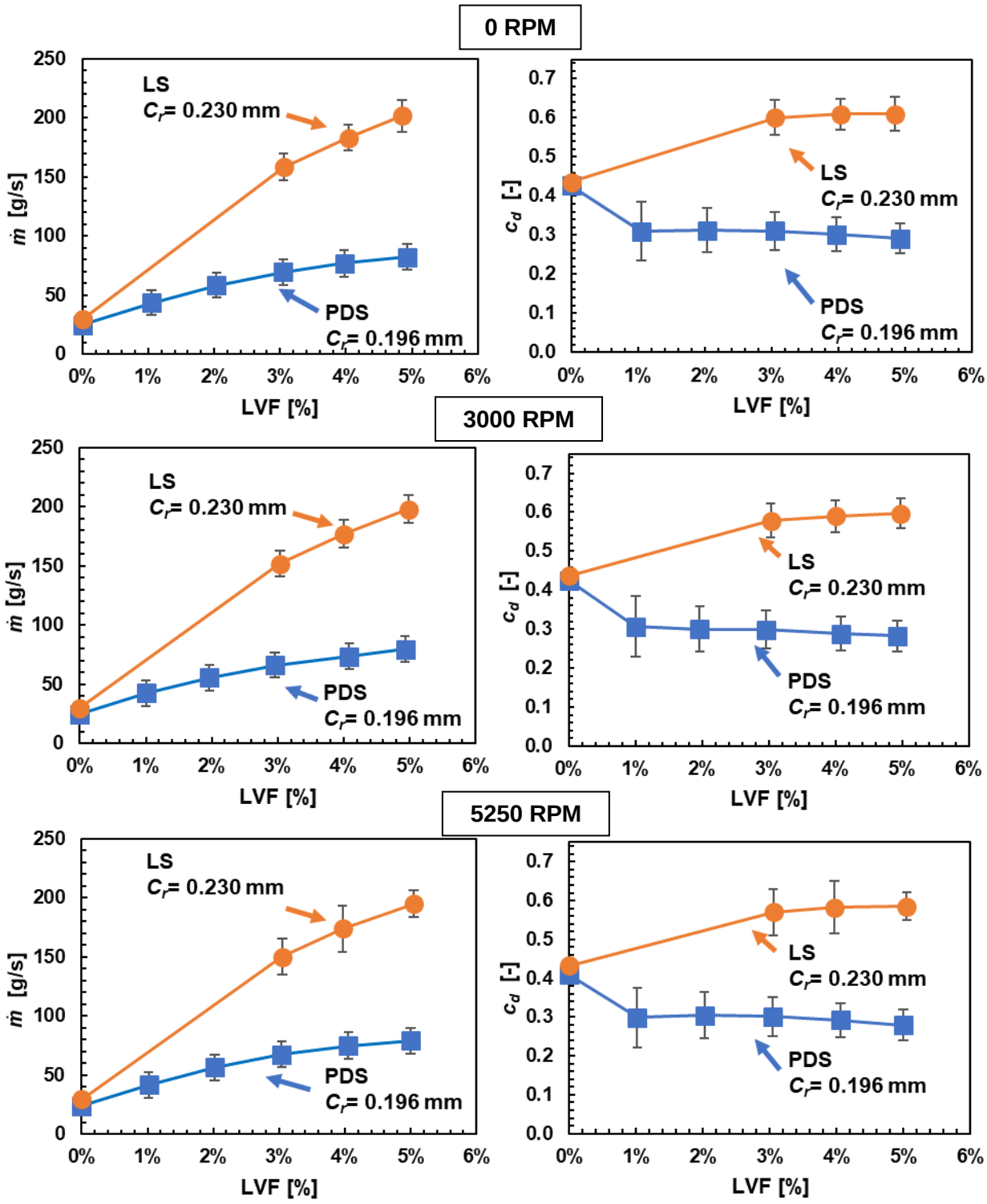

(a) Leakage, $\dot{m}$ **(b) Loss Coefficient, c_d**

Figure 7. PDS and LS: Leakage ($\dot{m}$) and loss coefficient (c_d) vs. inlet LVF. Operation with pressure ratio (P_s/P_e) = 2.5, and shaft speed = 0 rpm (top), 3,000 rpm (middle), and 5,250 rpm (bottom).

Characterization of Test Rig Structure Force Coefficients

The procedure to experimentally determine the rotordynamic force coefficients of a seal or bearing presented in Section 4 demands an experimental setup with only two degrees of freedom (see Figure 5). During experimentation, the author observed a resonance present in the shaker support structure (depicted in Figure 1) when the shakers excited the test rig at certain frequencies. The resonance occurs for low excitation frequencies (40, 50, and 60 Hz) and high excitation frequencies (110 and 120 Hz). Figure 8 presents the amplitude of the flexibility function ($G = 1/|H_{xx}|$) and phase angle ($Ø = \arctan[\mathrm{Im}(H_{xx})/\mathrm{Re}(H_{xx})]$) resulting from a series of dry runs (no flow through the test seal). Red circles depict the frequencies at which the shaker resonates, illustrating a discontinuity in the flexibility and phase angle. The vibrations in the shaker support structure introduce a new set of degrees of freedom into the system, thus invalidating the equations of motion presented by Eq. 12. All figures presenting rotordynamic force coefficients in this section intentionally skip the frequencies at which shaker resonance occurs, as well as the excitation frequency closest to the natural frequency of the test rig (80 Hz).

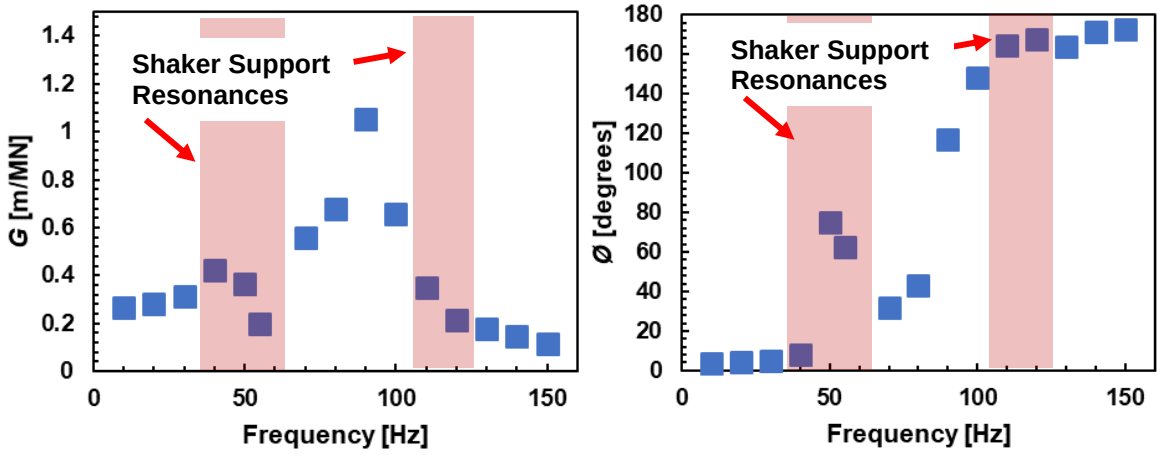

Figure 8. Amplitude (*G*) and phase angle (*Ø*) of test rig structure flexibility vs. excitation frequency (ω) under dry conditions (no flow condition).

Recall that the identification of the test seal dynamic stiffness requires subtraction of the test rig structure dynamic stiffness from the system total dynamic stiffness:

$$\mathbf{H}_{\text{Seal}(\omega)} = [\mathbf{H}_{(\omega)} - \mathbf{H}_{\text{Structure}(\omega)}] = \begin{bmatrix} H_{sys,xx} & H_{sys,xy} \\ -H_{sys,xy} & H_{sys,xx} \end{bmatrix} - \begin{bmatrix} H_{struc,xx} & H_{struc,xy} \\ -H_{struc,xy} & H_{struc,xx} \end{bmatrix} \quad (24)$$

A series of dynamic load tests performed under dry conditions (no flow through the test seal) provides the test rig structure dynamic stiffnesses. Figure 9 presents the real and imaginary parts of the test rig direct dynamic stiffness ($H_{struc,xx}$) and cross-coupled dynamic stiffness ($H_{struc,xy}$). The figure shows results for three cases of shaft speed, namely 0, 3,000, and 5,250 rpm. Note there is a slight decrease in both the real and imaginary parts of the structure dynamic stiffness as the shaft speed increases from 0 to 3,000 and 5,250 rpm. No firm explanation for the difference in test rig structure dynamic stiffness with respect to shaft speed is known. However, the variation of the structure dynamic stiffness with shaft speed suggests that a different set of baseline structure dynamic stiffness values should be used depending on the shaft speed set during experimentation. Table 3 lists the test rig direct stiffness (K), damping (C), and mass (M) coefficients resulting from the dynamic stiffness plotted in Figure 9.

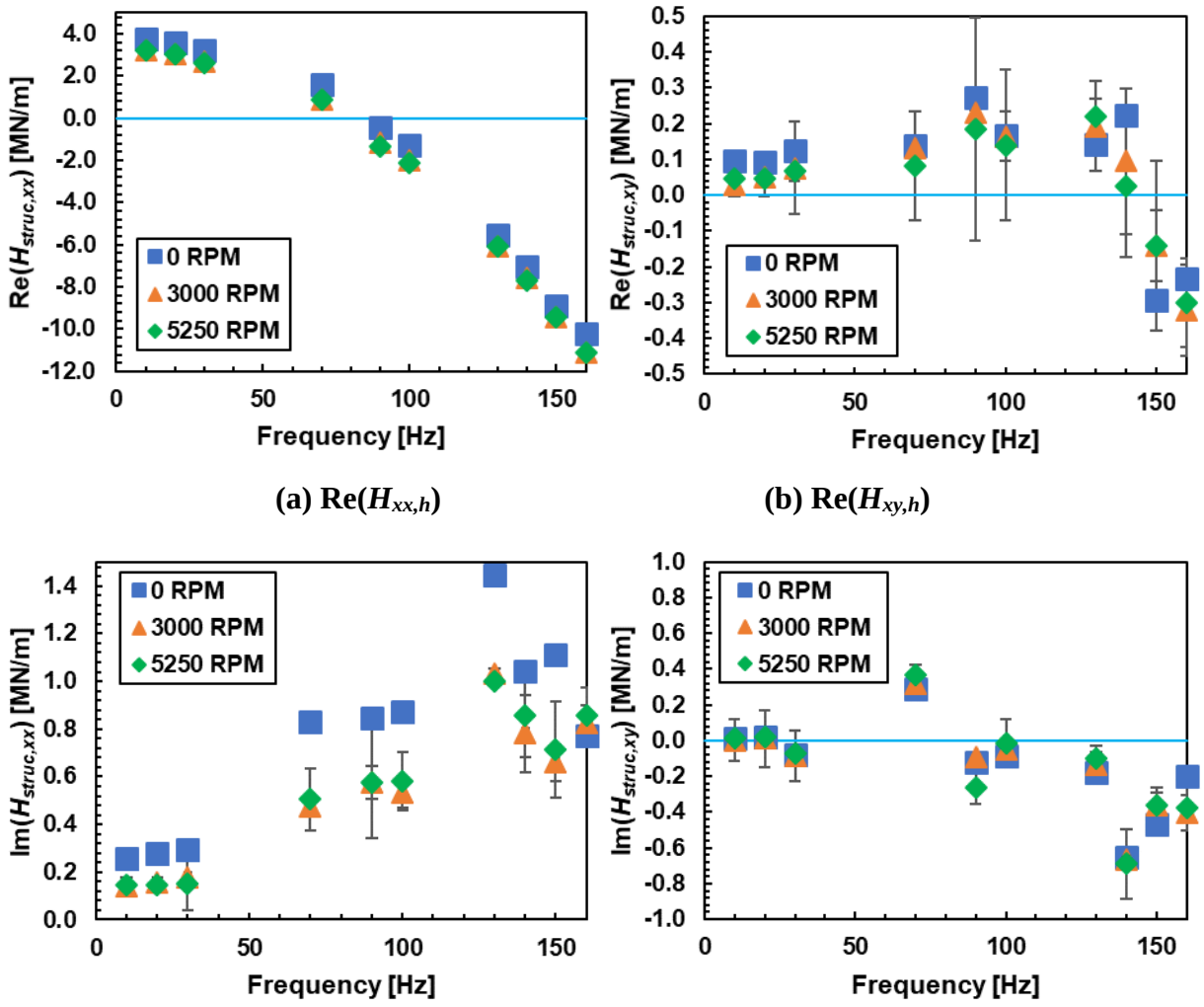

(a) Re($H_{xx,h}$) **(b) Re($H_{xy,h}$)**

(c) Im($H_{xx,h}$) **(d) Im($H_{xy,h}$)**

Figure 9. Test rig structure: Real and imaginary parts of direct dynamic stiffness ($H_{struc,xx}$) and cross-coupled dynamic stiffness ($H_{struc,xy}$) vs. excitation frequency.

Table 3. Test rig structure: Estimated stiffness (*K*), damping (*C*), and mass (*M*) coefficients.

Speed [rpm]	*K* [MN/m]	*C* [kN-s/m]	*M* [kg]	Seal Cartridge Mass [24]
0	3.96 ±0.02	1.26 ±0.02	14.13 ±0.07	14 kg
3,000	3.37 ±0.20	0.91 ±0.17	14.25 ±0.86	
5,250	3.30 ±0.06	0.95 ±0.16	14.19 ±0.85	

Rotordynamic Force Coefficients

Figure 10 presents the pocket damper seal (PDS) direct stiffness (K_{PDS}) and effective damping ($C_{eff,PDS}$) vs. excitation frequency for operation with a *wet* gas mixture. The inlet LVF equals 0%, 3%, and 5% (LMF = 0%, 90%, 94%), the shaft speed equals 0, 3,000, and 5,250 rpm, and the pressure ratio (P_s/P_e) = 2.5. Error bars in the graphs depict the experimental uncertainty of each identified parameter. The largest experimental uncertainty is ~ 3 MN/m for the direct stiffness and ~ 6 kN-s/m for the effective damping.

The results in Figure 10 show the pocket damper seal direct stiffness (K_{PDS}) is small in magnitude, often less than the total experimental uncertainty, regardless of excitation frequency. For operation with pure gas (LVF = 0%), K_{PDS} is small in magnitude (<0.2 MN/m) and positive. Note that as the mixture inlet LVF increases, K_{PDS} tends to decrease at low excitation frequencies (<50 Hz), most notably occurring with shaft speed equal to 0 rpm. K_{PDS} appears impervious to shaft speed, with the cases with shaft speed equal to 3,000 and 5,250 rpm appearing nearly identical.

Figure 10 reveals the magnitude of effective damping for the PDS ($C_{eff,PDS}$) varies greatly with the mixture inlet LVF. For operation with pure gas (LVF = 0%), $C_{eff,PDS}$ tends to be positive and low in magnitude (<1 kN-s/m), for all settings of shaft speed. For operation without shaft rotation, $C_{eff,PDS}$ increases as mixture LVF increases, most notably at low excitation frequencies (<50 Hz). Conversely, for operation with shaft speed equal to 3000 and 5250 rpm, $C_{eff,PDS}$ decreases significantly at excitation frequencies below 50 Hz and increases slightly at frequencies above 50 Hz.

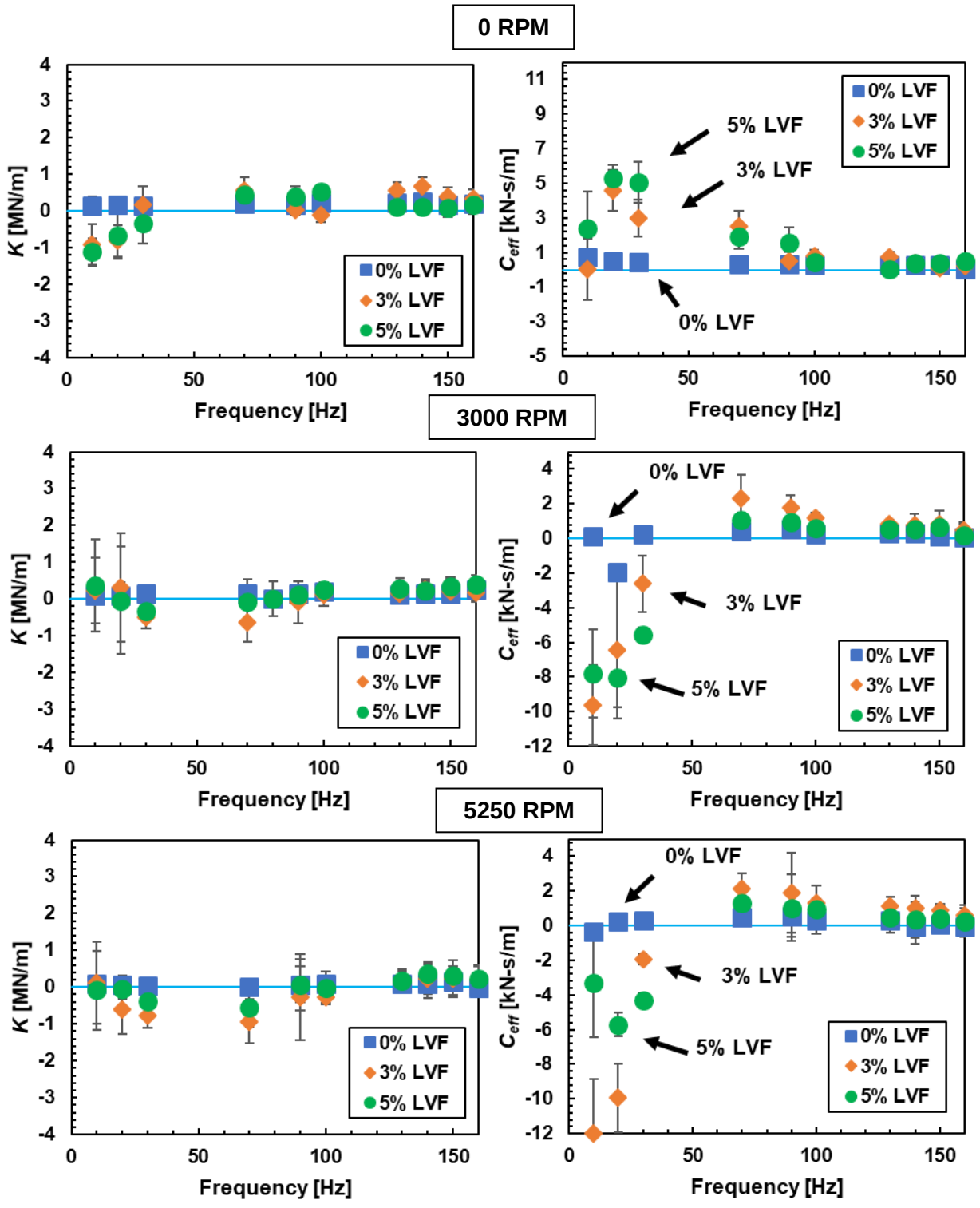

(a) Direct Stiffness, K (b) Effective Damping, C_{eff}

Figure 10. PDS: Direct stiffness (K) and effective damping (C_{eff}) vs. excitation frequency. Operation with inlet LVF = 0%, 3%, and 5%, and shaft speed = 0 rpm (top), 3,000 rpm (middle), and 5,250 rpm (bottom). Pressure ratio (P_s/P_e) = 2.5.

Figure 11 presents the direct stiffness (K) and effective damping (C_{eff}) coefficients vs. excitation frequency for the pocket damper seal (PDS) and the labyrinth seal (LS) for operation with pure gas (LVF = 0%), pressure ratio (P_s/P_e) equal to 2.5, and shaft speed equal to 0, 3,000, and 5,250 rpm. The maximum experimental uncertainty is ~ 1 MN/m for the direct stiffness and ~2 kN-s/m for the effective damping.

Figure 11 shows the direct stiffness of both the PDS and LS are small in magnitude, often less than the total experimental uncertainty. Note that although the magnitudes of direct stiffness of both seals are within the experimental uncertainty, K_{PDS} tends to produce a slightly larger direct stiffness than K_{LS} for tests conducted at three shaft speeds. Note K_{PDS} and K_{LS} appear impervious to both shaft speed and excitation frequency.

Figure 11 shows the effective damping coefficients for both the PDS and LS ($C_{eff,PDS}$, $C_{eff,LS}$) are small in magnitude (<2 kN-s/m). However, $C_{eff,PDS}$ is slightly larger than $C_{eff,LS}$, particularly for operation without shaft rotation. For operation with shaft rotation (Ω = 3,000 rpm, 5,250 rpm), the PDS and LS produce a nearly identical effective damping coefficient. Interestingly, the PDS produces $C_{eff,PDS} < 0$ when operating with shaft speed equal to 3,000 rpm and an excitation frequency equal to 20 Hz, and for shaft speed equal to 5,250 rpm and excitation frequency equal to 10 Hz.

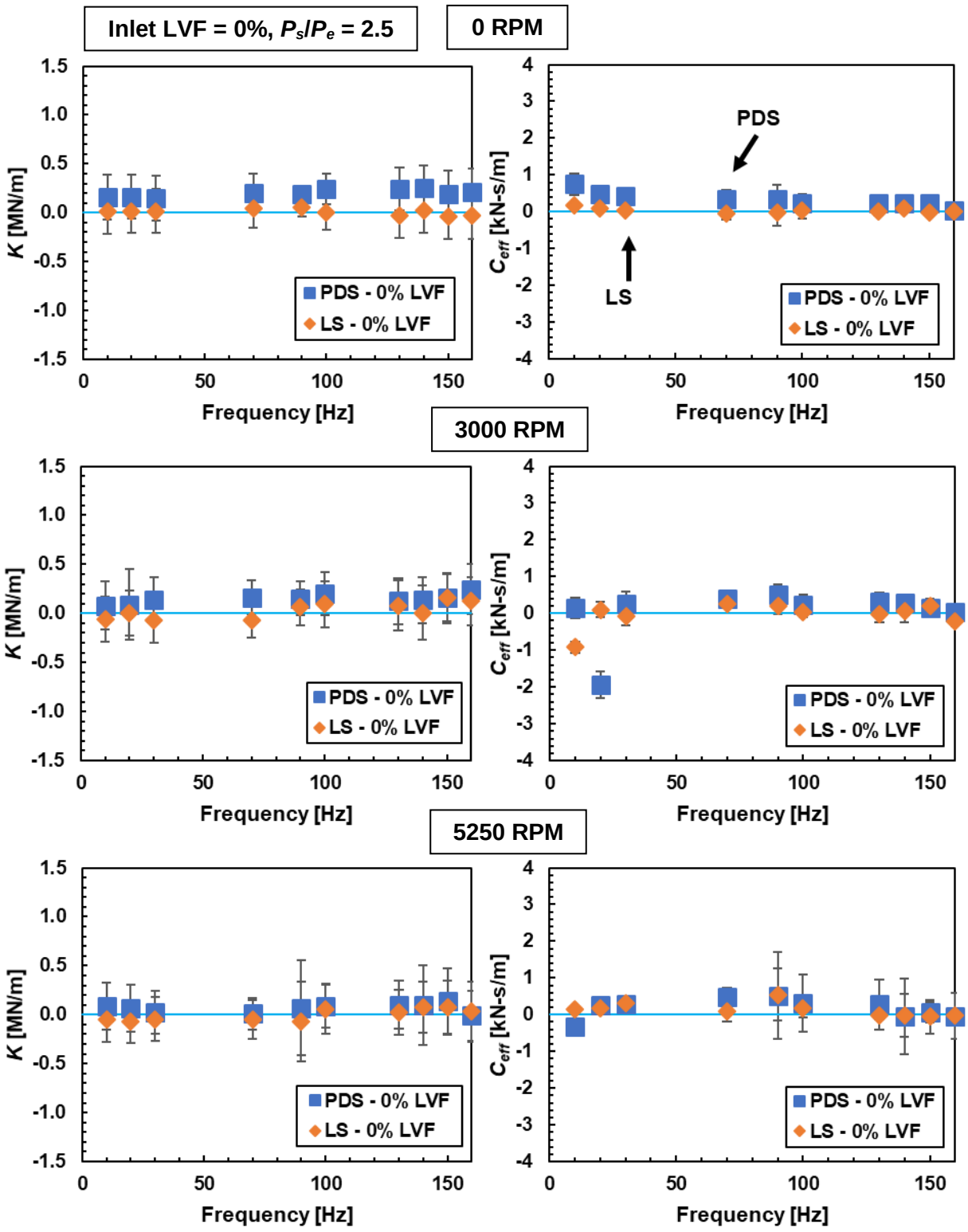

(a) Direct Stiffness, *K* **(b) Effective Damping, C_{eff}**

Figure 11. PDS and LS: Direct stiffness (*K*) and effective damping (C_{eff}) vs. excitation frequency. Operation with dry gas (LVF = 0%), and shaft speed = 0 rpm (top), 3,000 rpm (middle), and 5,250 rpm (bottom). Pressure ratio (P_s/P_e) = 2.5.

Figure 12 presents the direct stiffness (K) and effective damping (C_{eff}) coefficients vs. excitation frequency for the pocket damper seal (PDS) and labyrinth seal (LS) operating with inlet LVF equal to 3% (LMF = 90%), pressure ratio (P_s/P_e) equal to 2.5, and shaft speed equal to 0, 3,000, and 5,250 rpm. The maximum experimental uncertainty is ~ 3 MN/m for the direct stiffness and ~ 8 kN-s/m for the effective damping.

Figure 12 shows K_{PDS} and K_{LS} remain small in magnitude for operation with *wet* gas, similar as with operation with pure gas (LVF = 0%). The experimental results reveal a greater variability in K_{PDS} when compared to K_{LS} (as shown by the larger uncertainties). Nonetheless, the magnitude of K for both seals often remains smaller than the experimental uncertainty. Both K_{PDS} and K_{LS} appear unaffected by an increase in both shaft speed and excitation frequency.

Figure 12 illustrates the effective damping (C_{eff}) coefficients for the PDS and LS exhibit vastly different behavior when supplied with a *wet* gas. For operation without shaft rotation (Ω = 0 rpm), $C_{eff,PDS}$ is larger than $C_{eff,LS}$, with the difference between the two decreasing as the excitation frequency increases. One notable exception to this trend occurs at an excitation frequency of 10 Hz, in which C_{eff} for both seals is nearly zero. For operation with shaft rotation (Ω = 3,000 rpm, 5,250 rpm), $C_{eff,PDS} < 0$ for excitation frequencies less than 50 Hz. Meanwhile, $C_{eff,LS}$ remains very small, similar to the case without shaft rotation. Thus, in the presence of shaft rotation, the PDS produces a lesser effective damping than the LS does for excitation frequencies less than 50 Hz, and a greater effective damping for excitation frequencies greater than 50 Hz.

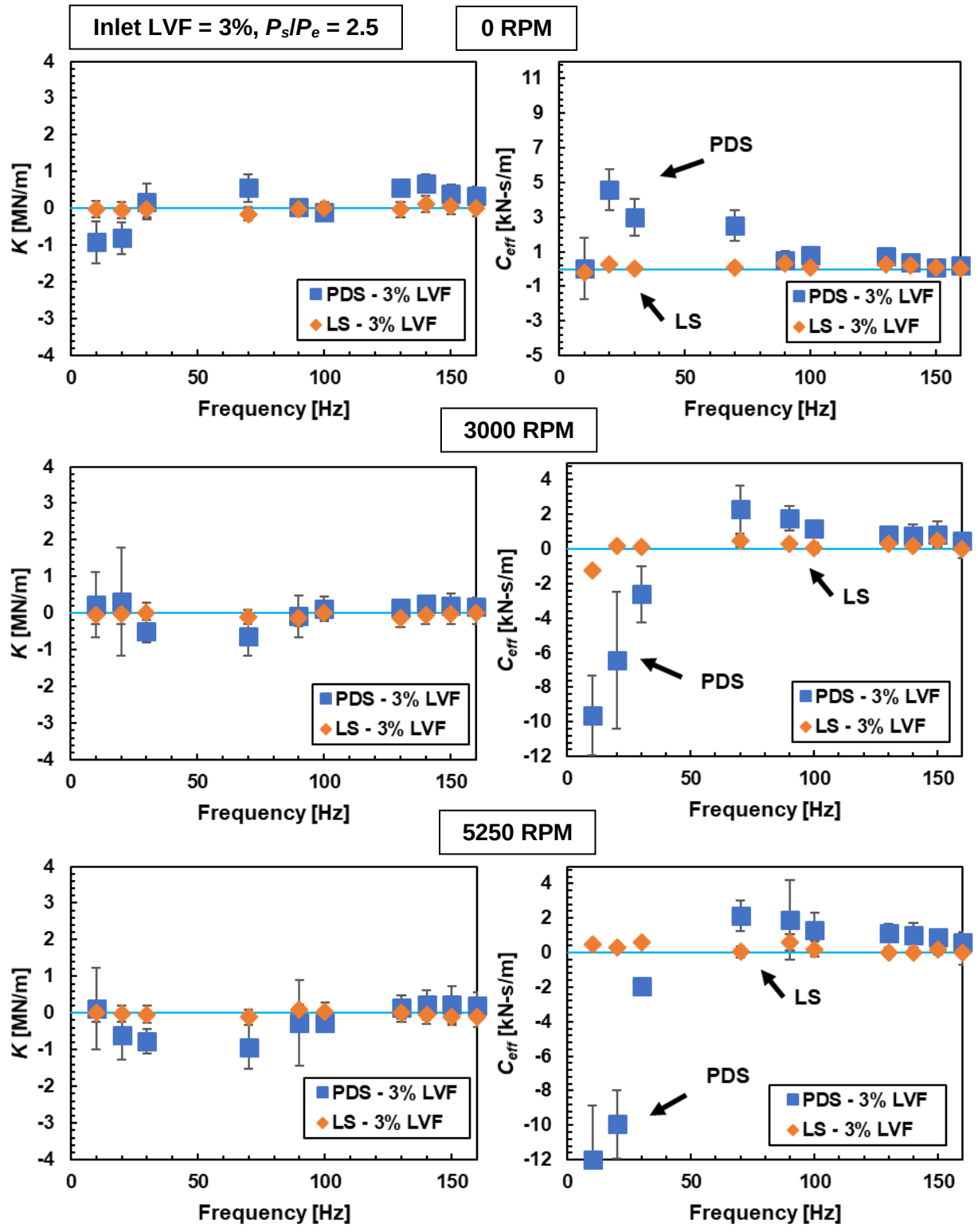

(a) Direct Stiffness, *K* **(b) Effective Damping, C_{eff}**

Figure 12. PDS and LS: Direct stiffness (*K*) and effective damping (C_{eff}) vs. excitation frequency. Operation with inlet LVF = 3%, and shaft speed = 0 rpm (top), 3,000 rpm (middle), and 5,250 rpm (bottom). Pressure ratio (P_s/P_e) = 2.5.

Figure 13 presents the direct stiffness (K) and effective damping (C_{eff}) vs. excitation frequency for the pocket damper seal (PDS) and labyrinth seal (LS) operating with inlet LVF equal to 5% (LMF = 94%), pressure ratio (P_s/P_e) equal to 2.5, and shaft speed equal to 0, 3,000, and 5,250 rpm. The maximum experimental uncertainty is ~ 3 MN/m for the direct stiffness and ~ 6 kN-s/m for the effective damping.

For operation with inlet LVF equal to 5%, K_{PDS} and K_{LS} remain unchanged when compared to the case of inlet LVF equal to 3%. Both seals produce a direct stiffness that is small in magnitude and often less than the experimental uncertainty. Note that K_{PDS} exhibits a greater variability as a result of the liquid phase, particularly noticeable at low excitation frequencies.

Figure 13 illustrates $C_{eff,PDS}$ and $C_{eff,LS}$ are different when operating with inlet LVF equal to 5%. $C_{eff,PDS}$ is greater than $C_{eff,LS}$ when operating without shaft rotation. Similar results are obtained for operation with inlet LVF equaling 3%. The difference between $C_{eff,PDS}$ and $C_{eff,LS}$ decreases as the excitation frequency increases. Conversely, for operation with shaft rotation (Ω = 3,000 and 5,250 rpm), $C_{eff,PDS}$ is negative when the seal is excited at a frequency less than 50 Hz. Meanwhile, $C_{eff,LS}$ shows a slight positive increase at low excitation frequencies (10 and 20 Hz) when shaft speed increases from 0 rpm to 3,000 or 5,250 rpm. The cross-over frequency, defined as the frequency at which the effective damping coefficient transitions from negative to positive, is of great important to design engineers. Figures 12 and 13 illustrate the PDS cross-over frequency is not greatly affected by an increase in LVF from 3% to 5%. Conversely, $C_{eff,LS}$ for operation with *wet* gas tends to remain positive and small in magnitude for the full range of excitation frequency.

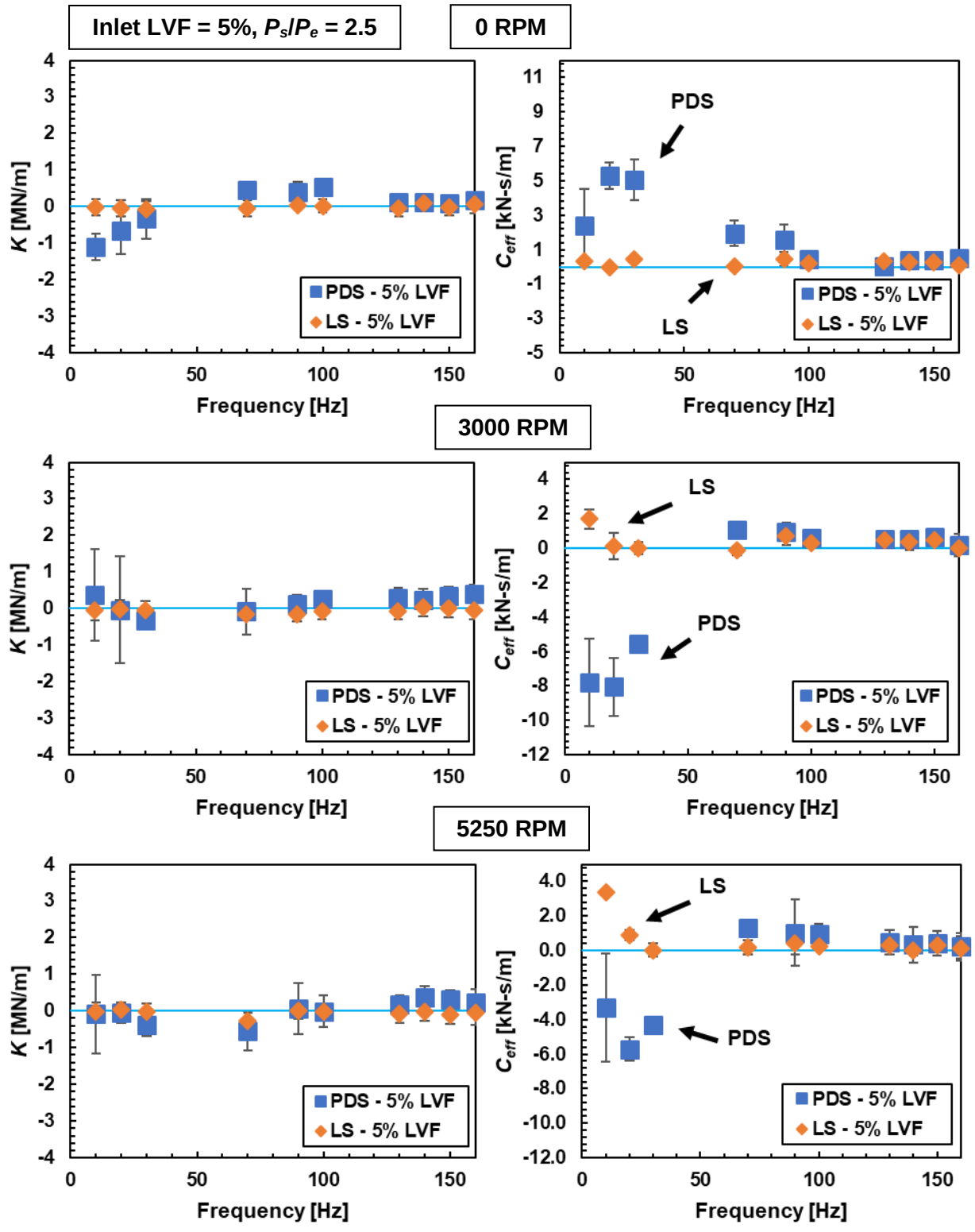

(a) Direct Stiffness, K (b) Effective Damping, C_{eff}

Figure 13. PDS and LS: Direct stiffness (K) and effective damping (C_{eff}) vs. excitation frequency. Operation with inlet LVF = 5%, and shaft speed = 0 rpm (top), 3,000 rpm (middle), and 5,250 rpm (bottom). Pressure ratio (P_s/P_e) = 2.5.

Comparison of Experimental Results (Pure Gas) to Predictions

This section presents a comparison of the measured results with predictions for the pocket damper seal (PDS) and labyrinth seal (LS) operating with pure gas. The predictions are generated using the XLTRC^2 software suite (XL_PDSeal and XLLaby). Figure 14 presents the experimental and predicted leakage vs. pressure ratio (P_s/P_e) for the PDS and LS operating with pure gas (LVF = 0%) and shaft speed equal to 5,250 rpm. The black and green lines depict the predicted leakage for the PDS and LS, respectively. Figure 14 illustrates the experimental results closely follow the predicted trends. The maximum deviation of experimental leakage from predicted leakage for the PDS is 4.9%, whereas the maximum deviation for the LS is only 3.1%.

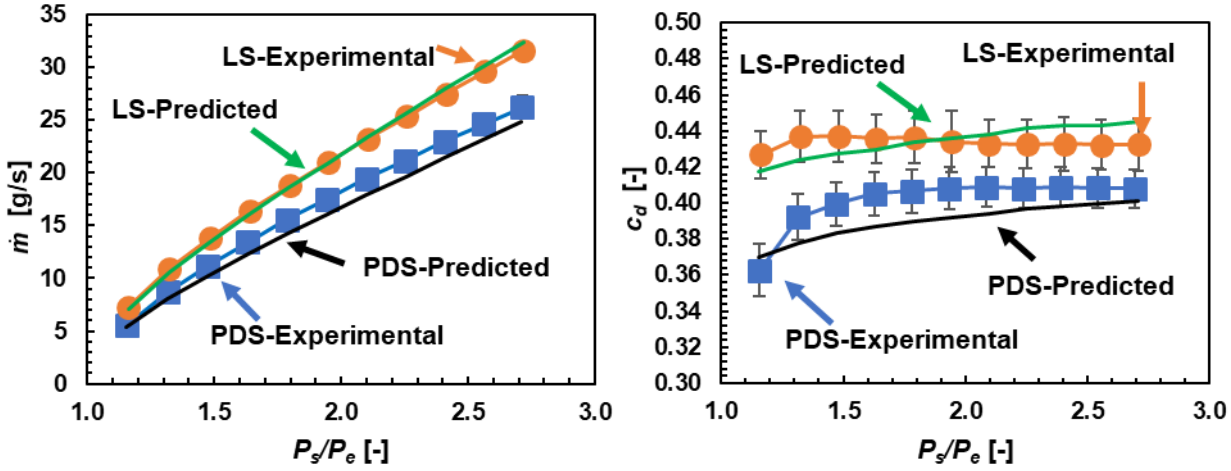

Figure 14. PDS and LS: Leakage ($\dot{m}$) and loss coefficient (c_d) vs. pressure ratio (P_s/P_e). Operation with pure gas (LVF = 0%) and shaft speed = 5,250 rpm. Comparison of test results to predictions.

Figure 15 presents the experimental and predicted direct stiffness (K) and effective damping (C_{eff}) for the PDS and LS operating with pure gas (LVF = 0%) and shaft speed equal to 0, 3,000, and 5,250 rpm. Error bars depict the uncertainty for each test data point. The majority of

the uncertainty in the experimental data results from precision uncertainty due to variability between samples, and the limited number of samples taken (only 3 tests performed per data point). Figure 15 shows the predicted direct stiffnesses (K) for the PDS and LS closely follow the experimental results. Note that the predictions estimate the PDS direct stiffness to remain constant with excitation frequency and equal 0.2 MN/m, regardless of shaft speed, whereas the LS direct stiffness is estimated to be near zero.

Figure 15 shows the predicted effective damping coefficients (C_{eff}) for the PDS and LS are near zero for operation without shaft speed. The experimental C_{eff} for the LS agrees well with the predicted results. However, the predictions underestimate the experimental C_{eff} for the PDS. As the shaft speed increases from 0 rpm to 3,000 and 5,250 rpm, the predictions estimate the PDS effective damping to decrease and the LS effective damping to increase.

The experimental results are not in agreement with the predictions, showing the PDS effective damping is generally greater than that of the LS. Note, however, that the experimental results have a large amount of uncertainty with respect to the magnitude of the results.

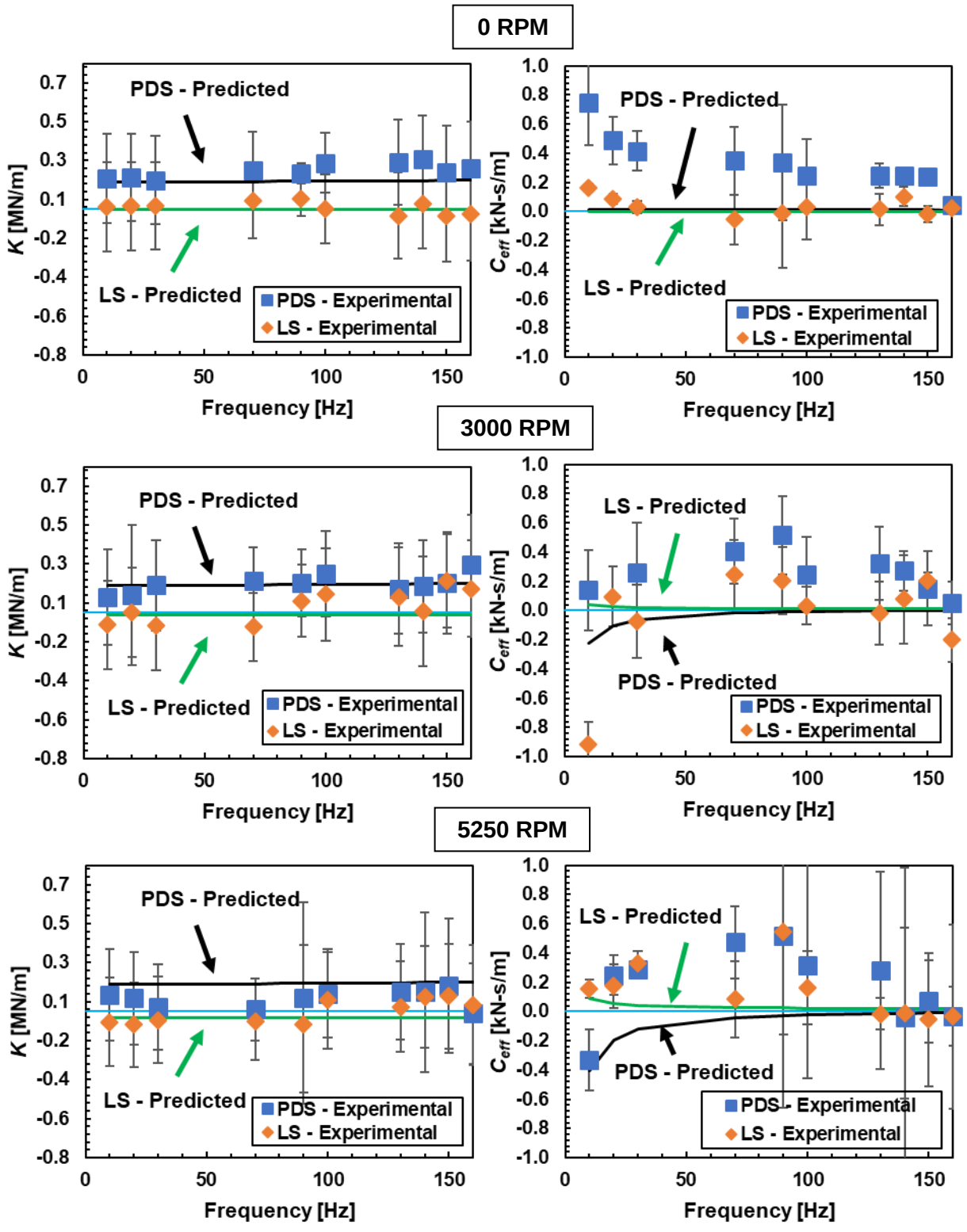

(a) Direct Stiffness, K **(b) Effective Damping, C_{eff}**

Figure 15. PDS and LS: Direct stiffness (K) and effective damping (C_{eff}) vs. excitation frequency. Operation with pure gas (LVF = 0%), and shaft speed = 0 rpm (top), 3,000 rpm (middle), and 5,250 rpm (bottom). Pressure ratio (P_s/P_e) = 2.5. Comparison of test results to predictions.

Evidence of Low Frequency Motions

Recall Vannini et al. [16] document the presence of unexpected subsynchronous vibrations (SSV) during operation of a *wet* gas LS with LVF ranging from 0% to 3%. The authors report the SSV occurring at 0.45X shaft speed with a maximum amplitude of vibration of nearly twice that of the shaft speed motion. The SSV disappear entirely when the LS is replaced with a similarly dimensioned PDS.

The current research yields finding that are in contradiction to those of Vannini et al. [16]. Figure 16 presents a surface plot illustrating the amplitude and frequency of vibrations for the seal cartridge over an elapsed time of 60 s while operating the PDS with a *wet* gas mixture, $P_s/P_e = 2.5$, and without shaft rotation. During the 60 s, the inlet LVF increases from 0% (gas only) to 5%, in steps of 1%, with each increment being held for 10 s. Figure 16 reveals that, when operating the PDS with *wet* gas, an unexpected broadband low frequency motion occurs. The amplitude of the motion worsens as the liquid content increases. For operation with pure gas (first 10 s in Figure 16), no low frequency motions are present, thus indicating the vibrations are caused by the presence of liquid in the mixture flowing through the seal. Figure 16 shows the maximum amplitude of the observed motion is approximately 5 μm, much lesser than the amplitude of the synchronous motion = 38 μm.

Figures 17 and 18 present the same experiment conducted with the PDS, while operating with shaft speed equal to 1,500 and 3,000 rpm, respectively. The results in both figures are nearly identical; both graphs reveal the low frequency motions increase in severity with the presence of shaft rotation. Although the maximum amplitude of the observed motion remains approximately 5 μm, the phenomenon appears to be more prevalent than the case without shaft rotation. Note the seal cartridge vibrations do not have components with frequencies greater than 100 Hz.

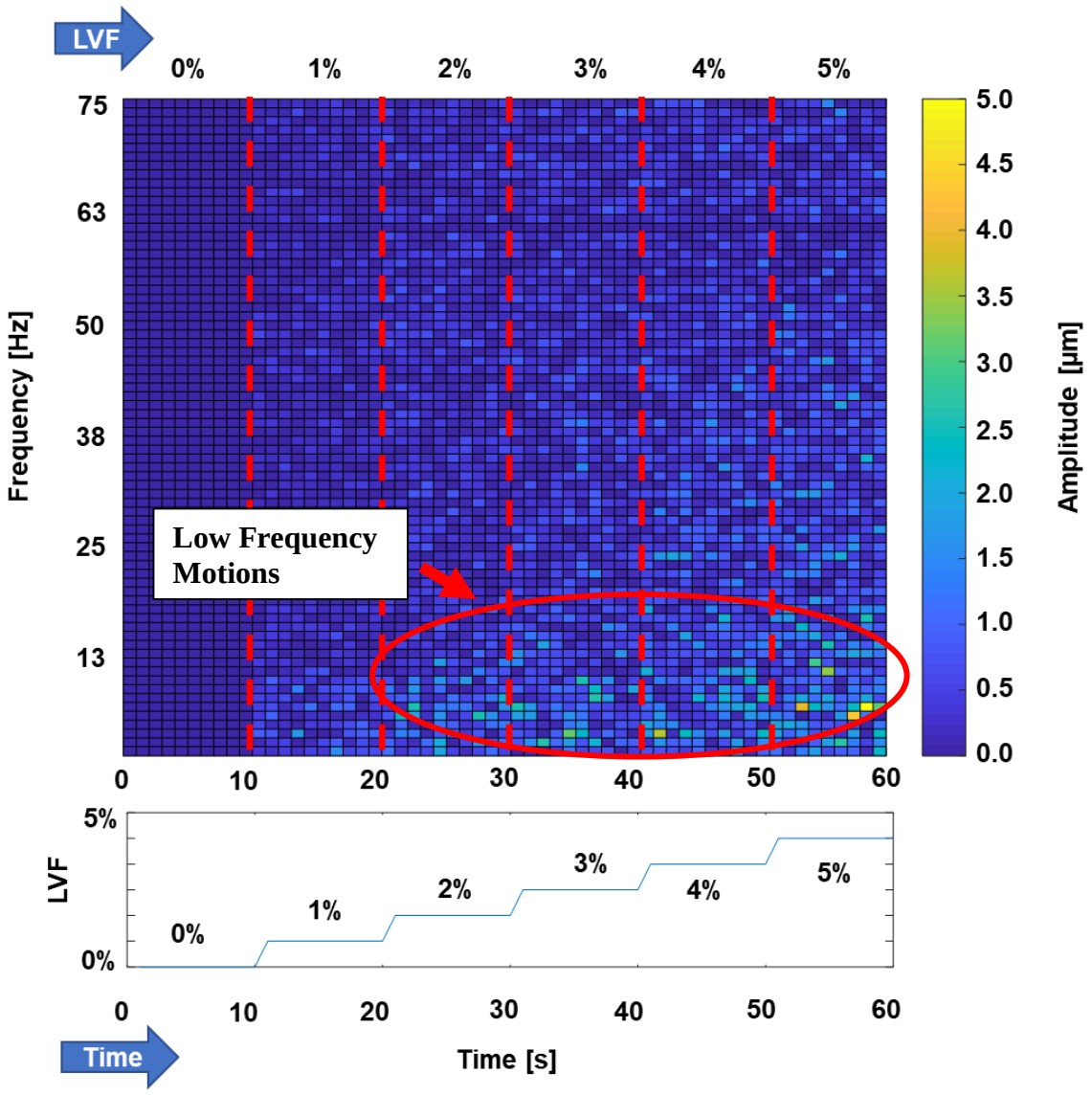

Figure 16. Color plot of amplitude of low frequency motions for a PDS operating without shaft rotation ($\Omega = 0$), $P_s/P_e = 2.5$, and inlet LVF ranging from 0% to 5% over an elapsed time of 60 s.

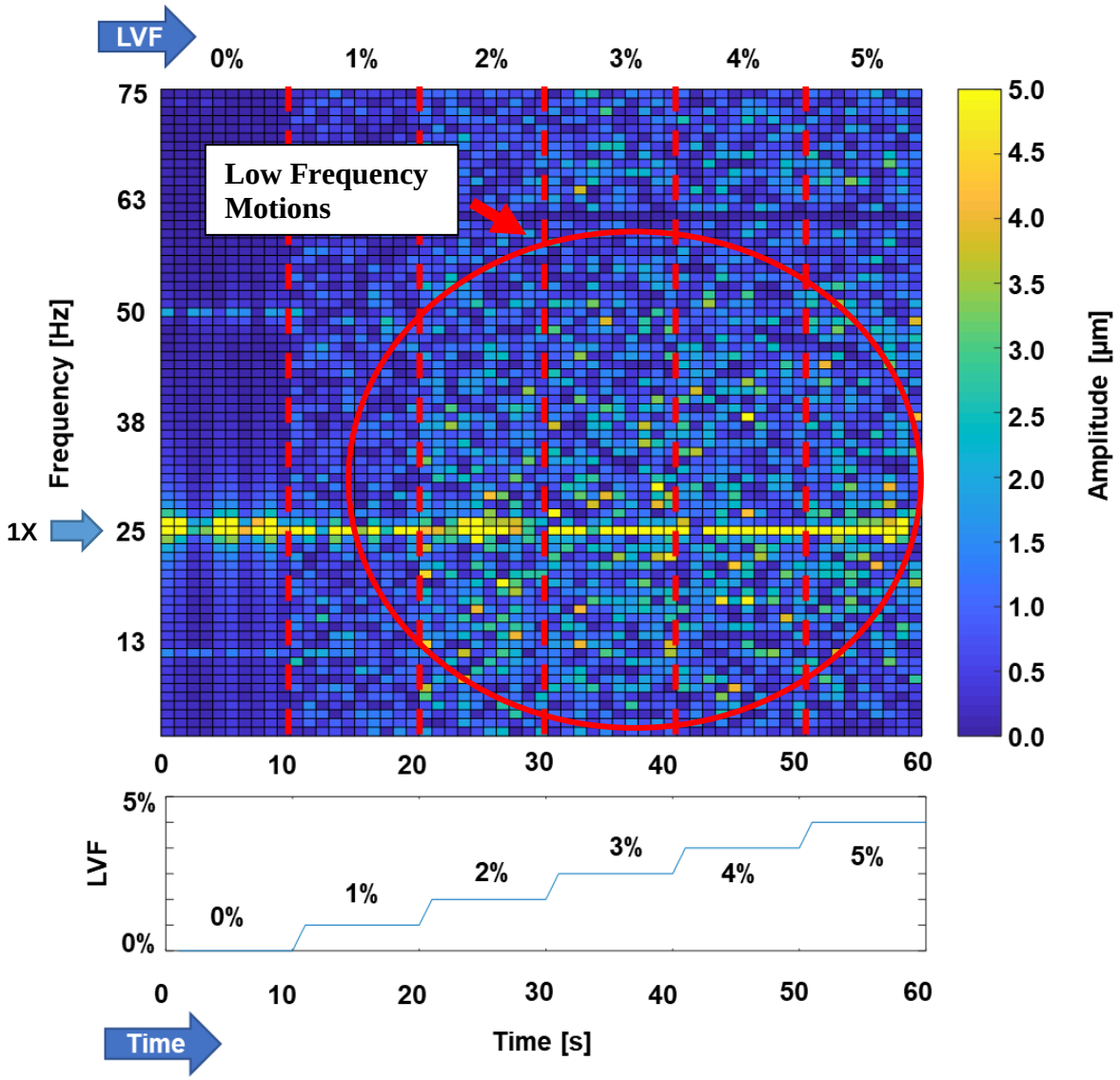

Figure 17. Color plot of amplitude of low frequency motions for a PDS operating with shaft speed equal to 1,500 rpm (25 Hz), P_s/P_e = 2.5, and inlet LVF ranging from 0% to 5% over an elapsed time of 60 s.

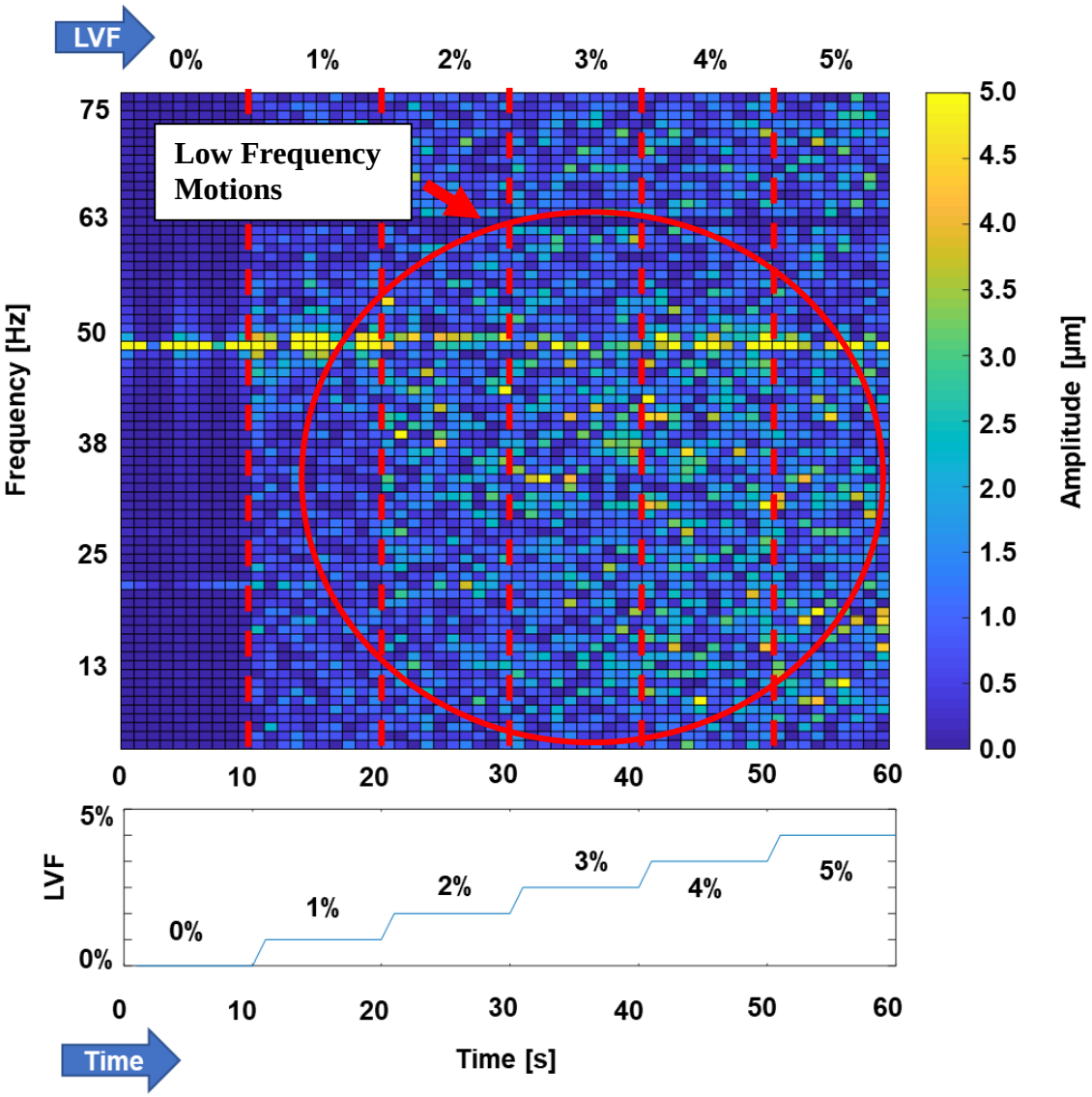

Figure 18. Color plot of amplitude of low frequency motions for a PDS operating with shaft speed equal to 3,000 rpm (50 Hz), P_s/P_e = 2.5, and inlet LVF ranging from 0% to 5% over an elapsed time of 60 s.

Figure 19 presents the same experiment conducted with the LS replacing the PDS. Interestingly, contrary to the results of Vannini et al. [16], the motions disappear entirely when replacing the PDS with the LS. Figure 19 presents the results for operation with a pressure ratio (P_s/P_e) equal to 2.5 and without shaft rotation, although results for operation with shaft speed equal to 1500 and 3000 rpm are nearly identical.

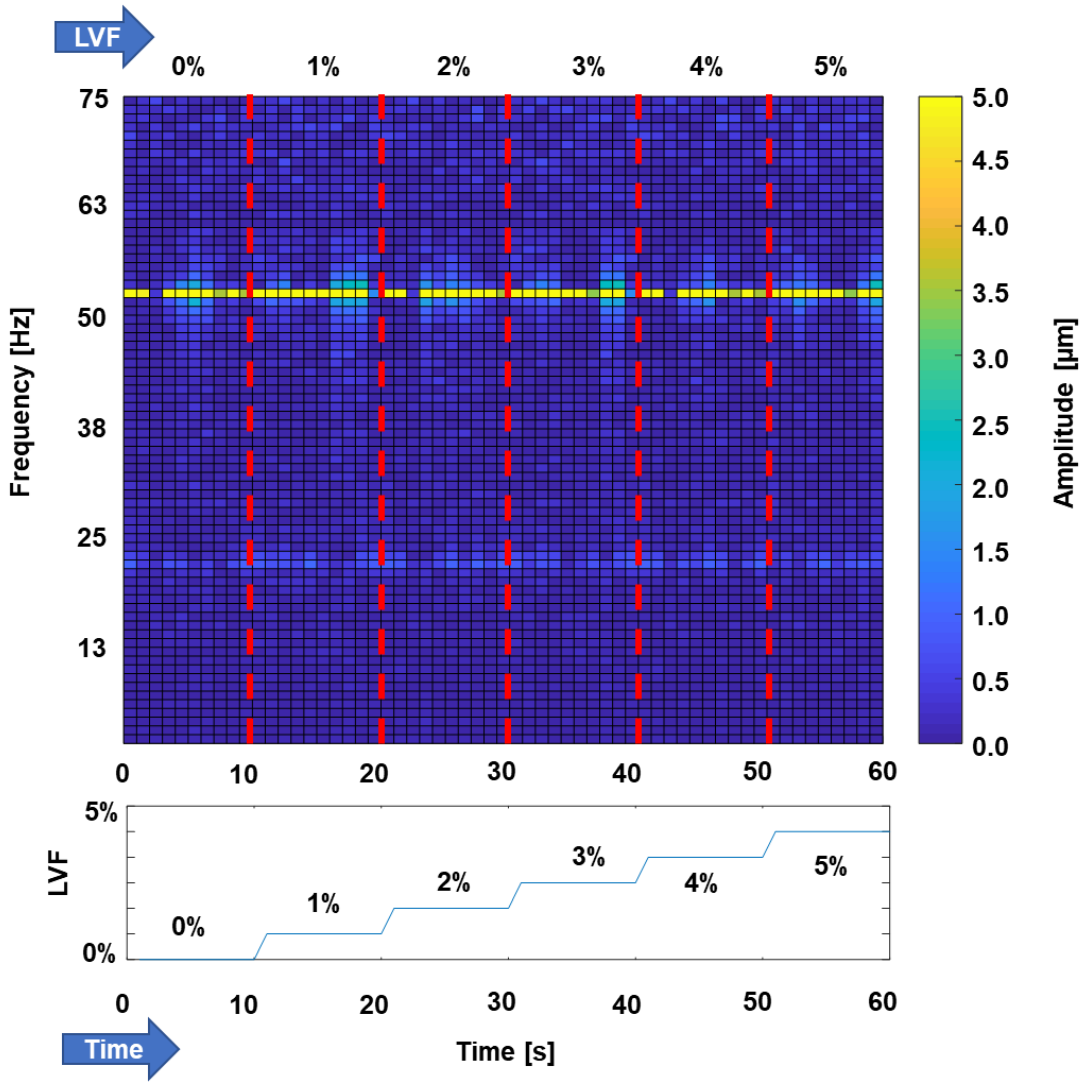

Figure 19. Color plot of amplitude of low frequency motions for a LS operating with shaft speed equal to 3,000 rpm (50 Hz), P_s/P_e = 2.5, and inlet LVF ranging from 0% to 5% over an elapsed time of 60 s. Similar results for operation with shaft speed equal to 0 and 1,500 rpm.

Investigation into Liquid Accumulation within PDS Pockets

The low frequency motions shown in the preceding section are unique to the PDS as they were not observed for operation with the LS. The vibrations are present only for operation with a *wet* gas mixture, with severity increasing as the inlet LVF of the mixture increases. A possible cause of the motion is the likelihood of liquid accumulating within the pockets of the PDS.

This section presents experiments conducted to determine whether liquid accumulation occurs when operating the PDS with a *wet* gas. A set of holes drilled into the PDS allow for bleeding the mixture of oil and air directly from the pockets, hence allowing for the estimation of the mixture LVF. A comparison of the estimated LVF with predicted magnitudes illustrates the likelihood of liquid accumulation.

Yang and San Andrés [36] present a simple analytical tool for the prediction of leakage and cavity pressures of LSs and PDSs operating with a two-phase flow. Estimation of cavity pressures arise from a simple iterative technique under the assumption of a homogenous mixture. The LVF at a particular cavity is a function of the cavity pressure (P), supply pressure (P_s), and inlet LVF (LVF_s) [36]:

$$\mathrm{LVF} = \frac{P_s \cdot \mathrm{LVF}_s}{P_s \cdot \mathrm{LVF}_s + (1 - \mathrm{LVF}_s) \cdot P} \tag{25}$$

Figure 20 illustrates the three holes drilled into the cavities of the test PDS, allowing access to bleed the *wet* gas mixture directly from the pockets of the PDS. Recall the test PDS comprises of four blades, sectioning the PDS into three axial cavities. Thus, there is one hole in each of the three pockets. Each hole contains 10-32 UNF-2B threads for installation of a fitting and ball valve.

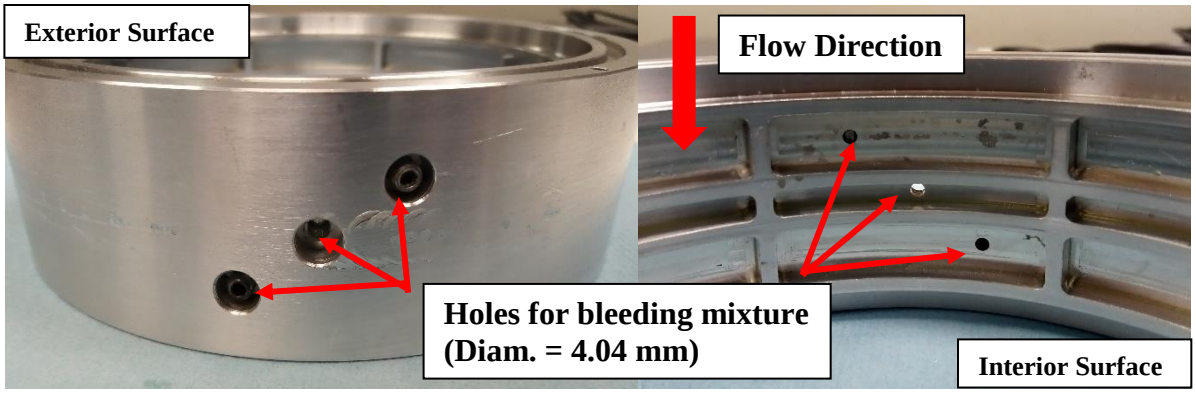

Figure 20. Images of exterior (left) and interior (right) radial faces of test PDS illustrating three holes for bleeding oil and air mixture from pockets.

Figure 21 illustrates the experimental setup for bleeding oil and air mixture from a pocket in the center cavity of the PDS. The experimental setup consists of three primary parts, a fitting with 10-32 UNF-2B threads, a simple ball valve, and a balloon. The fitting is attached directly to the hole in the PDS and contains 1/2-20 UNF 2B threads on the opposite end. A ball valve for starting and stopping the bleeding procedure is installed into the 1/2-20 threads. A balloon is secured to the opposite open end of the ball valve using a standard o-ring. During operation, the ball valve opens allowing the pressurized mixture of oil and air to fill the balloon.

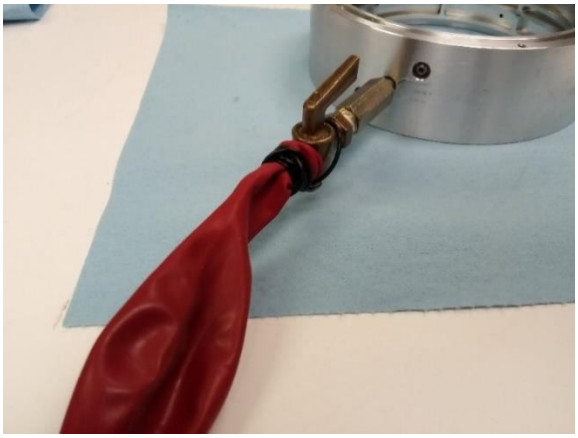

Figure 21. Image depicting ball valve and balloon setup used for bleeding oil and air mixture from PDS cavities.

The procedure for experimentally estimating the mixture LVF within the pockets of the PDS starts with supplying the test seal with a *wet* gas mixture (inlet LVF = 5%) at a pressure ratio (P_s/P_e) equal to 2.5. With the experimental setup, illustrated in Figure 21, installed into one of the three bleeding holes, the ball valve is opened for a total of five seconds. During the five seconds, the balloon fills with the pressurized mixture of oil and air. The LVF of the mixture within the balloon depends on the volume of the liquid (oil) inside the balloon and the total volume of the balloon. The total volume of the balloon ($V_{balloon}$) is estimated by submerging the balloon into a cylinder filled with oil and recording the subsequent rise in oil level. Figure 22 presents a schematic illustrating a balloon filled with a *wet* gas mixture being submerged into a cylinder filled with oil. Note the resulting rise in oil level is easily measured, and corresponds to the total volume of the balloon. A metal rod is used to secure the balloon to the bottom of the cylinder.

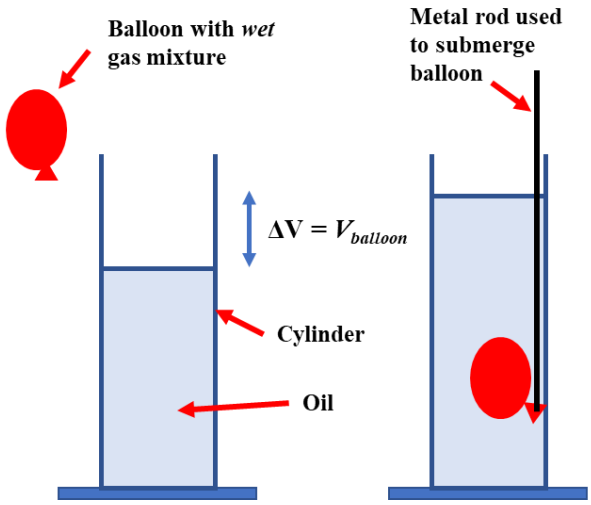

Figure 22. Schematic view illustrating equipment and process of measuring balloon volume ($V_{balloon}$).

The volume of the liquid within the balloon (V_{liquid}) depends on the mass of the liquid (m_{liquid}) and the known oil density (ρ_{oil}). Assuming the mass of the balloon and air are negligible, the mass of the liquid within the balloon is equal to the total mass of the balloon after the experiment and can be directly measured. Thus, the liquid volume follows by:

$$V_{liquid} = \frac{m_{liquid}}{\rho_{oil}} \tag{26}$$

With the volume of the liquid within the balloon and the total volume of the balloon known, the LVF of the mixture bled from the pockets of the PDS is

$$\text{LVF} = \frac{V_{liquid}}{V_{balloon}} \tag{27}$$

Table 4 summarizes the experimental and predicted LVF obtained at each of the three pockets of the PDS for operation with a supply LVF equal to 5%. Note that each experiment is performed three times for repeatability. Interestingly, the experimental LVF is lower than the predicted LVF for each of the three cavities, most notably occurring at the middle pocket in which the experiment LVF equals 2.9% compared to the predicted value of 3.7%. The lower experimental LVF values compared to the predictions indicates that liquid accumulation is likely not the cause of the SSVs observed in the previous section.

Table 4. Experimental and predicted LVF of *wet* gas mixture by pocket location.

		Top Pocket	Middle Pocket	Bottom Pocket
LVF [%]	**Experimental**	3.9	2.9	2.5
(Inlet LVF = 5%)	**Prediction**	4.2	3.7	2.9

Summary of Experimental Results with a Stepped Shaft Design

Torres et al. [40] present similar experimental work characterizing the leakage and rotordynamic force coefficients of a pocket damper seal (PDS) and labyrinth seal (LS) operating with a *wet* gas. The shaft features two steps aligned with the first and third blades of the PDS and LS, thus creating a local reduced clearance at the "step" locations. Figure 23 presents the design and dimensions of the stepped shaft seals. Note the clearance at the step locations are $C_{r,step\ PDS}$ = 0.106 mm and $C_{r,step\ LS}$ = 0.140, while the radial clearances at the non-step locations are $C_{r,PDS}$ = 0.196 mm and $C_{r,LS}$ = 0.230 mm. Aside from the inclusion of the shaft steps, the PDS and LS designs presented by Torres et al. [40] are otherwise identical to those already presented in this thesis.

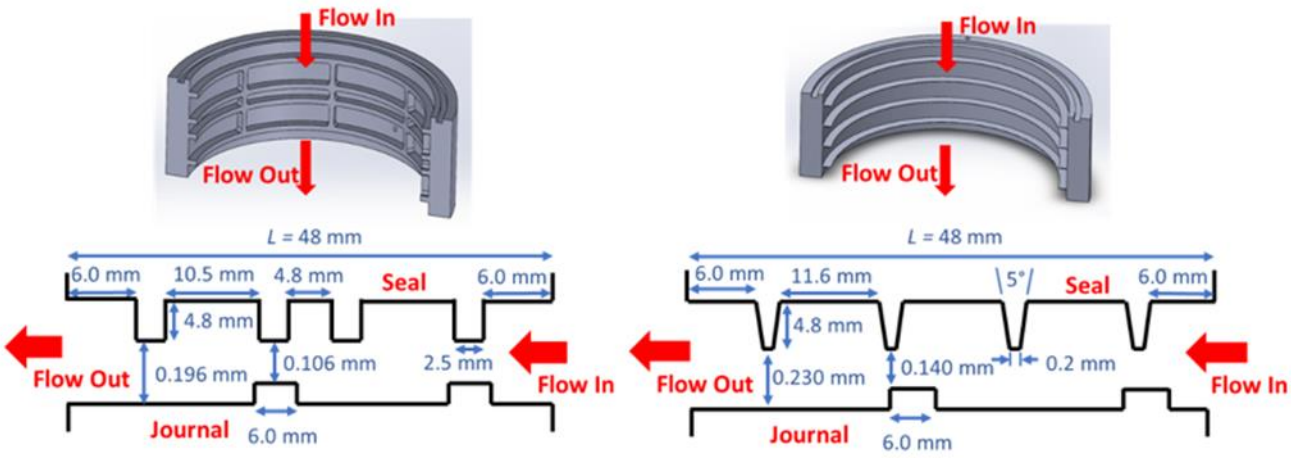

(a) stepped Pocket Damper Seal **(b) stepped Labyrinth Seal**

Figure 23. Cross-sectional diagrams illustrating dimensions of (a) stepped PDS and (b) stepped LS (Not to scale) [40].

Figure 24 presents the leakage ($\dot{m}$) and loss coefficient (c_d) of the stepped LS and stepped PDS vs. inlet LVF for operation with pressure ratio (inlet/exit) equal to 2.56 and shaft speed equal

to 5,250 rpm. Note that the stepped PDS c_d decreases as the inlet LVF increases while the stepped LS c_d increases as the inlet LVF increases. The stepped LS leaks significantly more than the stepped PDS when operating with a *wet* gas. The leakage shown in Figure 24 is similar to the results of the current research (see Figure 7), illustrating the PDS design is more effective in reducing *wet* gas leakage.

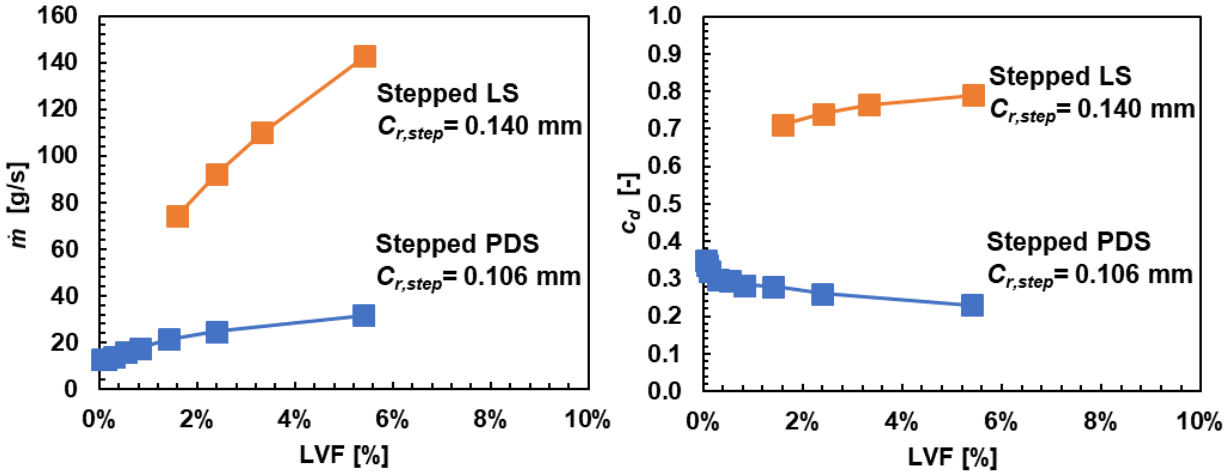

Figure 24. Stepped PDS and LS: Leakage ($\dot{m}$) and loss coefficient (c_d) vs. inlet LVF. Operation with pressure ratio (P_s/P_e) = 2.56, and shaft speed = 5,250 rpm.

Figure 25 presents the direct stiffness (K) and effective damping (C_{eff}) of the stepped PDS and stepped LS operating with a pressure ratio (P_s/P_e) equal to 2.35, journal speed equal to 5,250 rpm, and an inlet LVF equal to 1.3%. Similar to the uniform clearance PDS and LS direct stiffnesses presented in Figures 11 through 13, the stepped PDS and LS produce a direct stiffness that is low in magnitude. The stepped PDS produces a slight greater K than the LS for excitation frequencies above 50 Hz, while producing a negative K for frequencies below 50 Hz.

The effective damping (C_{eff}) of the stepped PDS follows a different trend than the C_{eff} of the uniform clearance PDS presented in Figures 11 through 13. Recall that when operating with a

wet gas and shaft speed equal to 5,250 rpm, the uniform clearance PDS produces a negative C_{eff} for excitation frequencies below 50 Hz and a positive C_{eff} for frequencies above 50 Hz. Conversely, Figure 25 reveals the stepped shaft produces a positive C_{eff} for all excitation frequencies when operating with a *wet* gas and with shaft speed equal to 5,250 rpm. Note, however, that the experiments presented by Torres et al. [40] are conducted with an inlet LVF = 1.3% and P_s/P_e = 2.35, whereas the results for the uniform clearance seals are conducted with an inlet LVF = 0%, 3%, and 5%, and P_s/P_e = 2.5. Further experimental work providing a direct comparison of the two seal configurations operating with identical inlet LVF and pressure ratio is needed.

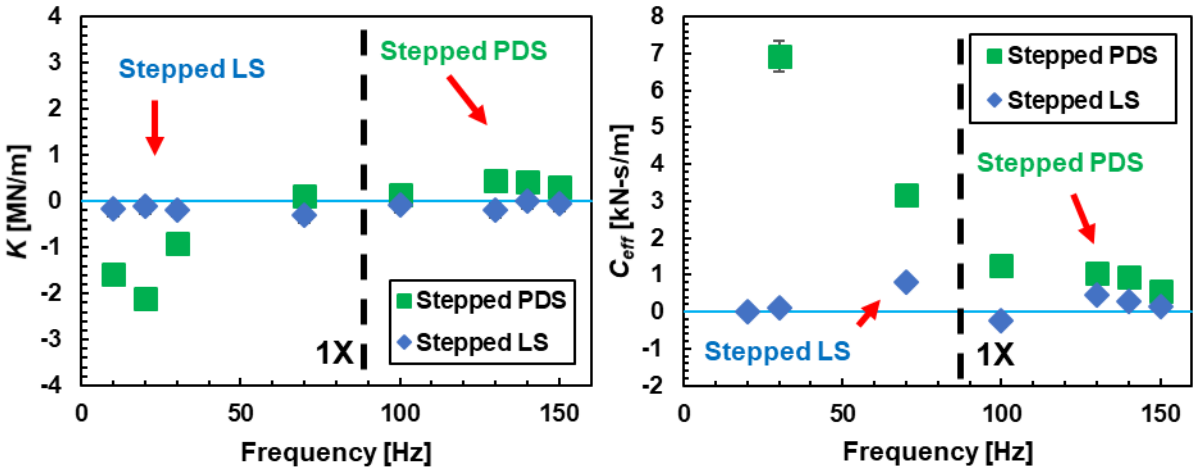

Figure 25. Stepped PDS and LS: Direct stiffness (K) and effective damping (C_{eff}) vs. excitation frequency. Operation with inlet LVF = 1.3%, and shaft speed = 5,250 rpm. Pressure ratio (P_s/P_e) = 2.35.

CONCLUSION

This thesis quantifies the leakage and rotordynamic force coefficients of a uniform clearance pocket damper seal (PDS) and a labyrinth seal (LS) operating with a *wet* gas mixture comprised of oil and air. The two seals have the same journal diameter, axial length, and number of cavities, although differing slightly in radial clearance due to a manufacturing error and a limited budget to procure a new seal. This work presents experimental results for operation with shaft speed equal to 0, 3,000, and 5,250 rpm (shaft surface speed = 0, 20, 35 m/s), pressure ratio (P_s/P_e) equal to 2.5, and a liquid volume fraction (LVF) ranging from 0% to 5% (liquid mass fraction = 0% - 94%). The major findings resulting from the experimental results obtained for the two seals are:

- For operation with pure gas, the LS leaks more due to a slightly larger radial clearance. Note that C_r = 0.230 mm for the LS and C_r = 0.196 mm for the PDS. However, the loss coefficient (c_d) is nearly identical for both seals, with the difference between the two being less than the experimental uncertainty. Recall c_d is a non-dimensional value, where a lower c_d indicates a more effective seal in reducing leakage.
- For operation with *wet* gas, as the inlet LVF increases, the c_d of the PDS decreases whereas the c_d of the LS increases. The leakage and loss coefficient of both seals appear insensitive to an increase in shaft surface speed up to 35 m/s.
- When operating with pure gas and an identical pressure ratio (P_s/P_e), the direct stiffness (K) and effective damping (C_{eff}) of both seals are small, often less than the experimental uncertainty.
- When operating with *wet* gas and an identical pressure ratio (P_s/P_e) and inlet LVF, the K of both seals remains small in magnitude for the three settings of shaft speed. When

operating without shaft rotation, the C_{eff} of the PDS is greater than that of the LS, particularly at low frequency excitations. Conversely, for operation with shaft speed equal to 3,000 and 5,250 rpm, the C_{eff} of the PDS is negative and lesser than that of the LS when excited at frequencies less than 50 Hz. When excited at frequencies greater than 50 Hz (> 1X), the PDS C_{eff} is positive and greater than that of the LS.

- The PDS produces unexpected low frequency whirl motions when operating with a *wet* gas. The motions increase in amplitude as shaft speed and inlet LVF increase. The low frequency motions are absent in tests performed with the LS. Although the motions could be a result of the negative effective damping ($C_{eff} < 0$) of the PDS when operating with *wet* gas, no firm explanation is yet known. Experiments in which *wet* gas mixture is bled directly from the pockets of the PDS rule out the possibility of liquid accumulation causing the low frequency motions.
- Torres et al. [40] present other experimental work testing a stepped shaft PDS. The shaft features two unique steps aligned with the blades of the PDS, creating a local reduced clearance at the "step" locations. The leakage and direct stiffness (K) results presented in this thesis follow the same basic trends as those in Ref. [40]. The stepped PDS, when operating with a *wet* gas mixture, produces a positive C_{eff} when the seal is excited at low frequencies (< 50 Hz). This differs from $C_{eff} < 0$ for the uniform clearance PDS under similar operating conditions hereby presented. Note, Torres et al. [40] conduct experiments with a maximum inlet LVF equal to 1.3%, whereas the present research utilizes a *wet* gas mixture with inlet LVF equal to 3% and 5%. Further experimental work providing a vis-à-vis comparison of the two seal configurations is recommended.

REFERENCES

[1] Childs, D.W., and Vance, J. M., 1997, “Annular Gas Seals and Rotordynamics of Compressors and Turbines,” Proc. of the 26th Turbomachinery Symposium, Houston, TX, September 16-18, pp. 201-220. https://doi.org/10.21423/R1HT06.

[2] Vance, J. M. and Schultz, R. R., 1993, “A New Damper Seal for Turbomachinery,” Proc. of the 14th Biennial Conference on Mechanical Vibration and Noise, Albuquerque, NM, September 19-22, pp 139-148. https://doi.org/10.1115/DETC1993-0188.

[3] Vance, J.M., and Li, J., 1996, “Test Results of a New Damper Seal in Vibration Reduction in Turbomachinery,” ASME J. Eng. Gas Turbines Power, **118**(10), pp. 843-846. https://doi.org/10.1115/1.2817004.

[4] Richards, R. L., Vance, J. M., Paquette, D. J., and Zeidan, F. Y., 1995, "Using A Damper Seal to Eliminate Subsynchronous Vibrations in Three Back-to-Back Compressors," Proc. of the 24th Turbomachinery Symposium, Houston, TX, September 26-28, pp. 59-71. https://doi.org/10.21423/R1MD4H.

[5] Ransom, D., Li, J., San Andrés, L., and Vance, J. M., 1999, "Experimental Force Coefficients for a Two-Bladed Labyrinth Seal and a Four-Pocket Damper Seal," ASME J. Tribol., **121**(4), pp. 370-376. https://doi.org/10.1115/1.2833949.

[6] Li, J., Kushner, F., and DeChoudhury, P., 2000, “Gas Damper Seal Test Results, Theoretical Correlation, and Applications in Design of High-Pressure Compressors,” Proc. of the 29th Turbomachinery Symposium, Houston, TX, September 18-21, pp. 55-64. https://doi.org/10.21423/R1BH29.

[7] Li, J., Kushner, F., and DeChoudhury, P., 2002, “Experimental Evaluation of Slotted Pocket Damper Seals on a Rotating Test Rig,” ASME Paper GT2002-30634. https://doi.org/10.1115/GT2002-30634.

[8] Ertas, B.H., and Vance, J.M., 2007, “Rotordynamic Force Coefficients for a New Damper Seal Design,” ASME J. Tribol., **129**(1), pp. 365-374. https://doi.org/10.1115/1.2464138.

[9] Sheng, N, Ruggiero, E. J., Devi, R., Guo, J., and Cirri, M., 2011 "Experimental and Analytical Leakage Characterization of Annular Gas Seals: Honeycomb, Labyrinth and Pocket Damper Seals." ASME Paper GT2011-45217. https://doi.org/10.1115/GT2011-45217.

[10] Delgado, A., Thiele, J., Cangioli, F., San Andrés, L., and Yang, J., 2020, “Rotordynamic Performance of a Fully-Partitioned Damper Seal: Experimental and Numerical Results,” Proc. of the 49th Turbomachinery Symposium, Houston, TX, December 8-10, pp. 1-29.

[11] Yang, J., San Andrés, L., Lu, X., 2021, “On the Leakage and Dynamic Force Coefficients of a Novel Stepped Shaft Pocket Damper Seal: Experimental and Numerical Verification,” ASME J. Eng. Gas Turbines Power, **143**(3), pp. 031002. https://doi.org/10.1115/1.4048459.

[12] Brenne, L., Bjorge, T., Gilarranz, J., Koch, J., and Miller, H., 2005, "Performance Evaluation of a Centrifugal Compressor Operating Under Wet Gas Conditions," Proc. of the 34th Turbomachinery Symposium, Houston, TX, September 16-18, pp. 111-120. https://doi.org/10.21423/R1V35Z.

[13] Musgrove, G., Poerner, M., and Bertoneri, M., 2014, "Overview of Important Considerations in Wet Gas Compression Testing and Analysis," Proc. of the 43rd Turbomachinery Symposium, Houston, TX, September 23-25. https://doi.org/10.21423/R1VD1J.

[14] Ransom, D., Podesta, L., Camatti, M., Wilcox, M., Bertoneri, M., and Bigi, M., 2011, "Mechanical Performance of a Two-Stage Centrifugal Compressor Under Wet Gas Conditions," Proc. of the 40th Turbomachinery Symposium, Houston, TX, September 12-15, pp. 121-128. https://doi.org/10.21423/R1NH1Q.

[15] Vannini, G, Bertoneri, M., Del Vescovo, G., and Wilcox, M., 2014, "Centrifugal Compressor Rotordynamics in Wet Gas Conditions," Proc. of the 43rd Turbomachinery Symposium, Houston, TX, September 23-25, pp. 201-220. https://doi.org/10.21423/R1F93J.

[16] Vannini, G., Bertoneri, M., Nielsen, K. K, Ludiciani, P., and Stronach, R., 2016, "Experimental Results and Computational Fluid Dynamics Simulations of Labyrinth and Pocket Damper Seals for Wet Gas Compression," ASME J. Eng. Gas Turbines Power, **138**(5), pp. 052501. https://doi.org/10.1115/1.4031530.

[17] San Andrés, L., Lu, X., and Jie, Z., 2018, "Leakage and Force Coefficients for Pump Annular Seals Operating with Air/Oil Mixtures: Measurements vs Predictions and Air Injection to Increase Seal Dynamic Stiffness" Second Asia Turbomachinery and Pump Symposium, The Turbomachinery Laboratory, Texas A&M University, Singapore, Mar. 13-15. https://hdl.handle.net/1969.1/175007.

[18] San Andrés, L., and Lu, X., 2018, "Leakage, Drag Power and Rotordynamic Force Coefficients of an Air in Oil (Wet) Annular Seal," ASME J. Eng. Gas Turbines Power, **140**(1), pp. 012505. https://doi.org/10.1115/1.4037622.

[19] Lu, X., and San Andrés, L., 2019, "Leakage and Rotordynamic Force Coefficients of a Three-Wave (Air in Oil) Wet Annular Seal: Measurements and Predictions," ASME J. Eng. Gas Turbines Power, **141**(3), pp. 032503. https://doi.org/10.1115/1.4041270.

[20] Zhang, M., Mclean, J. E., and Childs, D. W., 2017, "Experimental Study of the Static and Dynamic Characteristics of a Long Smooth Seal with Two-Phase, Mainly Air Mixtures," ASME J. Eng. Gas Turbines Power, **139**(12), pp. 122504. https://doi.org/10.1115/1.4037607.

[21] Shrestha, H., Childs, D. W., Tran, D. L., and Zhang, M., 2019, "Experimental Study of the Static and Dynamic Characteristics of a Long (L/D= 0.75) Labyrinth Annular Seal Operating under Two-Phase (Liquid/Gas) Conditions," ASME J. Eng. Gas Turbines Power, **141**(11), pp. 111002. https://doi.org/10.1115/1.4044309.

[22] Zhang, M., and Childs, D. W., 2020, "A Study for Rotordynamic and Leakage Characteristics of a Long-Honeycomb Seal with Two-Phase, Mainly Air Mixtures," ASME J. Eng. Gas Turbines Power, **142**(1), pp. 011021. https://doi.org/10.1115/1.4044947.

[23] Voigt, A.J., Mandrup-Poulsen, C., Nielson, K.K., and Santos, I.F., 2017 "Design and Calibration of a Full Scale Active Magnetic Bearing Based Test Facility for Investigating Rotordynamic Properties of Turbomachinery Seals in Multiphase Flow," ASME J. Eng. Gas Turbines Power, 139(5), pp. 052505. https://doi.org/10.1115/1.4035176.

[24] Yang, J., San Andrés, L., Lu, X., 2019, "Leakage and Dynamic Force Coefficients of a Pocket Damper Seal Operating Under a Wet Gas Condition: Tests Versus Prediction," ASME J. Eng. Gas Turbines Power, **141**(11), pp. 111001. https://doi.org/10.1115/1.4044307.

[25] Beatty, P.A., and Hughes, W.F., 1987, "Turbulent Two-Phase Flow in Annular Seals," Tribology Transactions, **30**(1), pp. 11-18. https://doi.org/10.1080/05698798708981724.

[26] Li, J., and San Andrés, L., 1999, "A Bulk-Flow Analysis of Multiple-Pocket Gas Damper Seals," ASME J. Eng. Gas Turbines Power, **121**(1), pp. 355-363. https://doi.org/10.1115/1.2817128.

[27] Li, J., and Vance, J.M., 1995, "Effects of Clearance and Clearance Ratio on Two and Three Bladed TAMSEALS," TRC-Seal-4-95. Turbomachinery Laboratory Research Progress Report, Texas A&M University, College Station.

[28] Li, J., Aguilar, R., San Andrés, L., and Vance, J. M, 2000, "Dynamic Force Coefficients of a Multiple-Blade, Multiple-Pocket Gas Damper Seal: Test Results and Predictions," ASME J. Tribol., **122**(1), pp. 317-322. https://doi.org/10.1115/1.555360.

[29] San Andres, L., 2011, "Rotordynamic Force Coefficients of Bubbly Mixture Annular Pressure Seals," ASME J. Eng. Gas Turbines Power, **134**(2), pp. 022503. https://doi.org/10.1115/1.4004130.

[30] Arghir, M., Zerarka, A., and Pineau, G., 2011, "Rotordynamic Analysis of Textured Annular Seals With Multiphase (Bubbly) Flow," Incas Bulletin, 3(3), pp. 3-13. https://doi.org/10.13111/2066-8201.2011.3.3.1.

[31] Hirs, G.G., 1973, "A Bulk-Flow Theory for Turbulence in Lubricant Films," ASME J. of Lubrication Tech., **95**(2), pp. 137-145. https://doi.org/10.1115/1.3451752.

[32] Brennen, C.E., 1995, *Cavitation and Bubble Dynamics*, Chapter 2, "Spherical Bubble Dynamics," Oxford University Press, New York, NY.

[33] San Andrés, L., Yang, J., and Lu, X., 2019, "On the Leakage, Torque, and Dynamic Force Coefficients of Air in Oil (Wet) Annular Seal: A Computational Fluid Dynamics Analysis Anchored to Test Data," ASME J. Eng. Gas Turbines Power, **140**(2), pp. 021008. https://doi.org/10.1115/1.4040766.

[34] Cangioli, F., Vannini, G., and Chirathadam, T., 2020, "A Novel Bulk-Flow Model for Pocket Damper Seals," ASME J. Eng. Gas Turbines Power, **142**(1), pp. 011012. https://doi.org/10.1115/1.4045000.

[35] Lu, X., San Andrés, L., and Yang, J., 2021, "A Nonhomogeneous Bulk Flow Model for Gas in Liquid Flow Annular Seals: An Effort to Produce Engineering Results," ASME Paper TRIB-21-1239, https://doi.org/10.1115/1.4052678.

[36] Yang, J., and San Andrés, L., 2021, "An Analytical Two-Phase Flow Model for Prediction of Leakage in Wet Gas Labyrinth Seals and Pocket Damper Seals. Is Simplicity Still Desired?" ASME J. Eng. Gas Turbines Power, **143**(12), pp. 121016. https://doi.org/10.1115/1.4051916.

[37] Childs, D. W., 1993, Turbomachinery Rotordynamics: Phenomena, Modeling, and Analysis, Chapter 5, "Rotordynamic Models for Annular Gas Seals," John Wiley & Sons, New York, NY.

[38] San Andrés, L., Wu, T., Barajas-Rivera, J., Zhang, J., and Kawashita, R., 2019, "Leakage and Cavity Pressures in an Interlocking Labyrinth Gas Seal: Measurements Versus Predictions," ASME J. Eng. Gas Turbines Power, **141**(10), pp 101007. https://doi.org/10.1115/1.4044284.

[39] San Andrés, L., 2009, *Modern Lubrication Theory*, "Experimental Identification of Bearing Force Coefficients," Notes 14, Texas A&M University Digital Libraries, [Mar 30, 2020], http://oaktrust.library.tamu.edu/handle/1969.1/93254, [Dec, 2021].

[40] Torres, J., San Andrés, L., and Yang, J., 2022, "A Stepped Shaft Labyrinth Seal vs. a Pocket Damper Seal: Leakage and Dynamic Force Coefficients Under Wet Gas Operation," ASME Paper GT2022-82280.

[41] Coleman, H. W., and Steele, W. G., 1989, Experimentation and Uncertainty Analysis for Engineers, Chapter 4, "Designing and Experiment: Detailed Uncertainty Analysis," John Wiley & Sons, New York, NY.

APPENDIX A

UNCERTAINTY ANALYSIS – LEAKAGE AND LOSS COEFFICIENT

The total uncertainty in the estimation of seal leakage and loss coefficient comprises of bias uncertainty and precision uncertainty. Bias uncertainty refers to the fixed and systematic error of each measurement that propagates into the final calculation, whereas precision uncertainty refers to the random component of the total error [41]. This appendix details the estimation of bias and precision uncertainties in estimating the seal leakage and loss coefficient.

Bias Uncertainty

Recall the total seal leakage ($\dot{m}$) of a *wet* gas mixture is the sum of the air and oil mass flow rates.

$$\dot{m} = \left(\rho_{oil} Q_{oil}\right) + \left(\rho_{air,s} Q_{air,s}\right) \tag{A1}$$

where ρ_{oil} and $\rho_{air,s}$ denote the oil and air density at the seal inlet, respectively, and Q_{oil} and $Q_{air,s}$ denote the oil and air volumetric flow rate at the seal inlet, respectively. The air flow meter displays the volumetric flow rate at standard conditions. Thus, the total seal leakage may alternatively be defined as

$$\dot{m} = \left(\rho_{oil} Q_{oil}\right) + \left(\rho_{stnd} Q_{air,recorded}\right) \tag{A2}$$

where ρ_{stnd} = 1.22 kg/m^3 denotes the density of air at the standard conditions (P_{stnd} = 101353 Pa, T_{stnd} = 288.88 K) defined by the manufacturer of the air flow meter. Thus, the total bias uncertainty in an estimate of seal leakage depends on the individual bias uncertainties of the oil and air flow meters. The oil density is treated as constant and thus does not contribute to the uncertainty. Note that for a pure gas flow (LVF = 0%), Eq. A2 is revised to omit the oil volumetric flow rate term.

Table 5 summarizes the individual bias uncertainties of the oil density, oil volumetric flow rate, and air volumetric flow rate. The bias uncertainties of the oil and air volumetric flow rates are specified by the manufacturers of the oil and air flow meters, respectively.

Table 5. Bias uncertainties for measurements of oil volumetric flow rate and air volumetric flow rate.

	Uncertainty
Oil Flow Rate, δQ_{oil}	0.2 gpm
Air Flow Rate, $\delta Q_{air,recorded}$	0.2 cfm

The propagation of bias errors into the estimation of seal leakage is given by [41]:

$$\delta \dot{m}_{bias} = \sqrt{\left(\frac{\partial \dot{m}}{\partial Q_{oil}} \delta Q_{oil} \right)^2 + \left(\frac{\partial \dot{m}}{\partial Q_{air,recorded}} \delta Q_{air,recorded} \right)^2} \tag{A3}$$

Note that the partial derivatives in Eq. A3 are evaluated using Eq. A2 and the recorded values corresponding to a particular data point. Thus, the bias uncertainty in the estimation of seal leakage varies between data points.

Recall the loss coefficient is a function of the recorded seal leakage and the ideal leakage through a single-restriction seal with radial clearance C_r. Thus, the bias uncertainty in the estimation of seal loss coefficient is a function of the total recorded leakage and the radial clearance of each seal. Note that the pressure drop across the seal, the journal diameter, and mixture density are identical for both test seals and treated as constants, and thus do not contribute to the loss coefficient bias uncertainty. The loss coefficient bias uncertainty is defined as

$$\delta c_{d,bias} = \sqrt{\left(\frac{\partial c_d}{\partial \dot{m}} \delta \dot{m}_{bias} \right)^2 + \left(\frac{\partial c_d}{\partial C_r} \delta C_r \right)^2} \tag{A4}$$

where δC_r = 0.005 mm denotes the bias uncertainty of the instrumentation used in measuring the seal radial clearance.

Precision Uncertainty

The precision error in the estimation of seal leakage is evaluated by performing multiple tests under identical operating conditions. Each data point presented in Section 5 represents an average of results among a total of three tests. The precision uncertainty of the average ($\delta\dot{m}_{prec}$) is estimated as [41]

$$\delta\dot{m}_{prec} = \frac{t_s S_{\dot{m}}}{\sqrt{N}} \tag{A5}$$

where N = 3 denotes the number of tests performed, $S_{\dot{m}}$ denotes the sample standard deviation, and t_s = 4.303 denotes the student's t-value corresponding to (N – 1) degrees of freedom and a 95% confidence interval.

Similarly, the precision error in the estimation of seal loss coefficient is given by

$$\delta c_{d,prec} = \frac{t_s S_{C_d}}{\sqrt{N}} \tag{A6}$$

Total Uncertainty

The total uncertainty in the estimation of seal leakage and loss coefficient with a 95% coverage are given by [41]:

$$\delta\dot{m}_{total} = \sqrt{\left(\delta\dot{m}_{bias}\right)^2 + \left(\delta\dot{m}_{prec}\right)^2} \tag{A7}$$

$$\delta c_{d,total} = \sqrt{\left(\delta c_{d,bias}\right)^2 + \left(\delta c_{d,prec}\right)^2} \tag{A8}$$

Tables 6 and 7 presents the results and corresponding total uncertainties for the seal leakage and loss coefficients results presented in Figs. 6 and 7, respectively.

Table 6. Experimental results and total uncertainties (δ) for estimation of seal leakage (Figures 6 and 7).

	Pocket Damper Seal, LVF = 0% (Figure 6 results)						**Labyrinth Seal, LVF = 0% (Figure 6 results)**					
	Ω = 0 rpm		**Ω = 3000 rpm**		**Ω = 5250 rpm**		**Ω = 0 rpm**		**Ω = 3000 rpm**		**Ω = 5250 rpm**	
P_s/P_e	$\dot{m}$ [g/s]	$\delta\dot{m}_{total}$ [g/s]	$\dot{m}$ [g/s]	$\delta\dot{m}_{total}$ [g/s]	$\dot{m}$ [g/s]	$\delta\dot{m}_{total}$ [g/s]	$\dot{m}$ [g/s]	$\delta\dot{m}_{total}$ [g/s]	$\dot{m}$ [g/s]	$\delta\dot{m}_{total}$ [g/s]	$\dot{m}$ [g/s]	$\delta\dot{m}_{total}$ [g/s]
1.16	5.5	0.5	5.5	0.4	5.3	0.2	7.3	0.4	7.4	0.3	7.3	0.7
1.32	8.7	0.5	8.7	0.4	8.3	0.2	10.9	0.4	11.0	0.3	10.9	0.3
1.47	11.2	0.4	11.3	0.4	10.7	0.2	13.8	0.4	13.8	0.5	13.8	0.3
1.63	13.5	0.4	13.5	0.4	12.9	0.2	16.4	0.5	16.5	0.4	16.3	0.4
1.79	15.6	0.6	15.6	0.4	14.8	0.2	18.8	0.5	18.9	0.5	18.7	0.5
1.94	17.5	0.3	17.6	0.5	16.7	0.2	21.1	0.5	21.1	0.3	20.9	0.7
2.10	19.5	0.3	19.4	0.5	18.5	0.1	23.2	0.5	23.3	0.4	23.1	0.5
2.25	21.2	0.7	21.1	1.1	20.3	0.1	25.4	0.5	25.5	0.4	25.2	0.6
2.41	23.0	0.7	22.9	1.1	22.0	0.1	27.5	0.5	27.6	0.4	27.3	0.7
2.56	24.6	0.6	24.6	1.2	23.6	0.2	29.6	0.5	29.8	0.3	29.4	0.7
2.71	26.2	1.1	26.3	1.3	25.3	0.1	31.6	0.6	31.8	0.4	31.5	0.8
	Pocket Damper Seal, P_s/P_e = 2.5 (Figure 7 results)						**Labyrinth Seal, P_s/P_e = 2.5 (Figure 7 results)**					
	Ω = 0 rpm		**Ω = 3000 rpm**		**Ω = 5250 rpm**		**Ω = 0 rpm**		**Ω = 3000 rpm**		**Ω = 5250 rpm**	
LVF	$\dot{m}$ [g/s]	$\delta\dot{m}_{total}$ [g/s]	$\dot{m}$ [g/s]	$\delta\dot{m}_{total}$ [g/s]	$\dot{m}$ [g/s]	$\delta\dot{m}_{total}$ [g/s]	$\dot{m}$ [g/s]	$\delta\dot{m}_{total}$ [g/s]	$\dot{m}$ [g/s]	$\delta\dot{m}_{total}$ [g/s]	$\dot{m}$ [g/s]	$\delta\dot{m}_{total}$ [g/s]
5%	82.1	6.0	79.5	5.7	79.1	5.9	201.3	10.2	197.8	7.3	194.8	6.4
4%	76.6	6.0	73.5	5.8	74.6	6.4	183.1	6.4	176.8	7.3	173.6	17.5
3%	69.2	5.5	66.0	5.7	67.3	6.4	158.1	6.4	151.7	6.1	150.0	12.3
2%	58.2	5.3	55.5	5.7	56.3	5.7						
1%	43.4	5.3	42.3	5.6	41.6	5.8						

Table 7. Experimental results and total uncertainties (δ) for estimation of seal loss coefficient (c_d) (Figures 6 and 7).

	Pocket Damper Seal, LVF = 0% (Figure 6 results)						**Labyrinth Seal, LVF = 0% (Figure 6 results)**					
	Ω = 0 rpm		**Ω = 3000 rpm**		**Ω = 5250 rpm**		**Ω = 0 rpm**		**Ω = 3000 rpm**		**Ω = 5250 rpm**	
P_s/P_e	c_d [-]	$\delta c_{d,total}$ [-]	c_d [-]	$\delta c_{d,total}$ [-]	c_d [-]	$\delta c_{d,total}$ [-]	c_d [-]	$\delta c_{d,total}$ [-]	c_d [-]	$\delta c_{d,total}$ [-]	c_d [-]	$\delta c_{d,total}$ [-]
1.16	0.38	0.04	0.38	0.03	0.36	0.01	0.42	0.03	0.43	0.02	0.43	0.01
1.32	0.41	0.03	0.41	0.02	0.39	0.01	0.44	0.02	0.44	0.02	0.44	0.01
1.47	0.42	0.02	0.42	0.02	0.40	0.01	0.44	0.02	0.44	0.02	0.44	0.01
1.63	0.42	0.02	0.42	0.02	0.41	0.01	0.44	0.02	0.44	0.01	0.44	0.01
1.79	0.43	0.02	0.43	0.02	0.41	0.01	0.44	0.01	0.44	0.02	0.44	0.01
1.94	0.43	0.01	0.43	0.02	0.41	0.01	0.44	0.01	0.44	0.01	0.43	0.02
2.10	0.43	0.01	0.43	0.01	0.41	0.01	0.44	0.01	0.44	0.01	0.43	0.01
2.25	0.43	0.02	0.42	0.02	0.41	0.01	0.44	0.01	0.44	0.01	0.43	0.01
2.41	0.43	0.02	0.43	0.02	0.41	0.01	0.44	0.01	0.44	0.01	0.43	0.01
2.56	0.43	0.02	0.42	0.02	0.41	0.01	0.44	0.01	0.44	0.01	0.43	0.01
2.71	0.42	0.02	0.42	0.02	0.41	0.01	0.43	0.01	0.44	0.01	0.43	0.01
	Pocket Damper Seal, P_s/P_e = 2.5 (Figure 7 results)						**Labyrinth Seal, P_s/P_e = 2.5 (Figure 7 results)**					
	Ω = 0 rpm		**Ω = 3000 rpm**		**Ω = 5250 rpm**		**Ω = 0 rpm**		**Ω = 3000 rpm**		**Ω = 5250 rpm**	
LVF	c_d [-]	$\delta c_{d,total}$ [-]	c_d [-]	$\delta c_{d,total}$ [-]	c_d [-]	$\delta c_{d,total}$ [-]	c_d [-]	$\delta c_{d,total}$ [-]	c_d [-]	$\delta c_{d,total}$ [-]	c_d [-]	$\delta c_{d,total}$ [-]
5%	0.29	0.04	0.28	0.04	0.28	0.04	0.61	0.04	0.60	0.04	0.58	0.04
4%	0.30	0.04	0.29	0.04	0.29	0.04	0.61	0.04	0.59	0.04	0.58	0.07
3%	0.31	0.05	0.30	0.05	0.30	0.05	0.60	0.04	0.58	0.04	0.57	0.06
2%	0.31	0.06	0.30	0.06	0.30	0.06						
1%	0.31	0.08	0.31	0.08	0.30	0.08						

APPENDIX B

UNCERTAINTY ANALYSIS –FORCE COEFFICIENTS

The total uncertainty in the estimation of rotordynamic force coefficients comprises of bias uncertainty and precision uncertainty. Bias uncertainty refers to the fixed and systematic error of each measurement that propagates into the final calculation of seal leakage, whereas precision uncertainty refers to the random component of the total error [41]. This appendix details the estimation of bias and precision uncertainties in the estimation of force coefficients.

Bias Uncertainty

The dynamic stiffness is dependent on the recorded seal displacement with respect to the rigid rotor, the seal absolute acceleration, and the load applied to the seal cartridge. Thus, the individual bias uncertainties of the eddy current displacement probes, piezoelectric accelerometers, and load cells propagate into the bias uncertainty of the dynamic stiffness. Table 8 summarizes the bias uncertainty of the aforementioned instrumentation.

Table 8. Bias uncertainties for measurements of seal displacement, acceleration, and applied load.

	Uncertainty
Displacement, δD	4.0 kg/m^3
Acceleration, δA	0.2 gpm
Load, δF	0.2 cfm

The propagation of bias errors into the calculation of dynamic stiffness is estimated as:

$$\delta H_{ij,bias} = \left|H_{ij}\right| \sqrt{\left(\frac{\delta \mathbf{D}}{\mathbf{D}_{measured}}\right)^2 + \left(\frac{\delta \mathbf{A}}{\mathbf{A}_{measured}}\right)^2 + \left(\frac{\delta \mathbf{F}}{\mathbf{F}_{measured}}\right)^2} \quad \text{(B1)}$$

where $\mathbf{D}_{measured}$, $\mathbf{A}_{measured}$, and $\mathbf{F}_{measured}$ denote the amplitude of the measured periodic displacement, acceleration, and applied load, respectively.

Precision Uncertainty

The precision error in the estimation of dynamic stiffness is evaluated by performing multiple tests under identical operating conditions. Each data point presented in Section 5 represents an average of results among a total of three tests. The precision uncertainty of the average ($\delta H_{ij,prec}$) is estimated as [41]

$$\delta H_{ij,prec} = \frac{t_s S_{H_{ij}}}{\sqrt{N}} \tag{B2}$$

where N = 3 denotes the number of tests performed, $S_{H_{ij}}$ denotes the sample standard deviation, and t_s = 4.303 denotes the student's t-value corresponding to (N – 1) degrees of freedom and a 95% confidence interval.

Total Uncertainty

The total uncertainty in the estimation of dynamic stiffness for a 95% coverage is given by [41]:

$$\delta H_{ij,total} = \sqrt{\left(\delta H_{ij,bias}\right)^2 + \left(\delta H_{ij,prec}\right)^2} \tag{B3}$$

Note that the direct stiffness (K) and effective damping (C_{eff}) are functions of the real and imaginary parts of the dynamic stiffness (H_{ij}):

$$K = \text{Real}(H_{xx}) \tag{B4}$$

$$C_{eff} = C - k/\omega = [\text{Ima}(H_{xx}) - \text{Real}(H_{xy})]/\omega \tag{B5}$$

Thus, the total uncertainty in the estimation of direct stiffness and effective damping for a given set of operating conditions is

$$\delta K_{total} = \delta H_{ij,total} \tag{B6}$$

$$\delta C_{eff,total} = \sqrt{\left(\frac{\partial C_{eff}}{\partial H_{xx}}\delta H_{xx}\right)^2 + \left(\frac{\partial C_{eff}}{\partial H_{xy}}\delta H_{xy}\right)^2} \tag{B7}$$

Tables 9, 10, and 11 summarize the direct stiffness (K) and effective damping (C_{eff}) values and total uncertainties corresponding to the results presented in Section 5 for operation with inlet LVF equal to 0%, 3%, and 5%, respectively. Note that the direct stiffness for both seals operating with pure gas is often small in comparison to the experimental uncertainty. Thus, the corresponding value is approximately zero, indicating the magnitude is too small for accurate measurement. For operation with *wet* gas, the PDS direct stiffness magnitude tends to increase, while the LS direct stiffness magnitude remains approximately zero.

Table 9. Experimental results and total uncertainties (δ) for estimation of direct stiffness and effective damping (Figure 11).

Inlet LVF = 0%

	Pocket Damper Seal											
	Ω = 0 rpm				**Ω = 3000 rpm**				**Ω = 5250 rpm**			
ω	**K [MN/m]**	**δK_{total} [MN/m]**	**C_{eff} [kN-s/m]**	**$\delta C_{eff,total}$ [kN-s/m]**	**K [MN/m]**	**δK_{total} [MN/m]**	**C_{eff} [kN-s/m]**	**$\delta C_{eff,total}$ [kN-s/m]**	**K [MN/m]**	**δK_{total} [MN/m]**	**C_{eff} [kN-s/m]**	**$\delta C_{eff,total}$ [kN-s/m]**
10	~ 0	0.23	0.75	0.29	~ 0	0.25	~ 0	0.28	~ 0	0.24	-0.33	0.21
20	~ 0	0.23	0.49	0.16	~ 0	0.36	-1.93	0.35	~ 0	0.24	0.25	0.14
30	~ 0	0.23	0.41	0.14	~ 0	0.23	~ 0	0.34	~ 0	0.22	0.29	0.04
70	~ 0	0.20	0.35	0.23	~ 0	0.17	0.41	0.23	~ 0	0.16	0.47	0.25
90	0.19	0.05	~ 0	0.40	~ 0	0.17	0.51	0.27	~ 0	0.49	~ 0	1.18
100	0.24	0.16	~ 0	0.25	~ 0	0.22	~ 0	0.26	~ 0	0.23	~ 0	0.78
130	0.24	0.22	0.24	0.08	~ 0	0.23	0.32	0.25	~ 0	0.25	~ 0	0.67
140	0.26	0.23	0.24	0.05	~ 0	0.24	0.27	0.14	~ 0	0.41	~ 0	1.02
150	~ 0	0.24	0.24	0.04	~ 0	0.26	~ 0	0.26	~ 0	0.34	~ 0	0.28
160	~ 0	0.24	0.04	0.02	~ 0	0.26	~ 0	0.15	~ 0	0.26	~ 0	0.63
	Labyrinth Seal											
	Ω = 0 rpm				**Ω = 3000 rpm**				**Ω = 5250 rpm**			
ω	**K [MN/m]**	**δK_{total} [MN/m]**	**C_{eff} [kN-s/m]**	**$\delta C_{eff,total}$ [kN-s/m]**	**K [MN/m]**	**δK_{total} [MN/m]]**	**C_{eff} [kN-s/m]**	**$\delta C_{eff,total}$ [kN-s/m]**	**K [MN/m]**	**δK_{total} [MN/m]**	**C_{eff} [kN-s/m]**	**$\delta C_{eff,total}$ [kN-s/m]**
10	~ 0	0.23	0.16	0.03	~ 0	0.23	-0.91	0.15	~ 0	0.23	0.15	0.06
20	~ 0	0.23	0.09	0.03	~ 0	0.23	~ 0	0.21	~ 0	0.22	0.17	0.15
30	~ 0	0.22	~ 0	0.04	~ 0	0.23	~ 0	0.25	~ 0	0.22	0.33	0.08
70	~ 0	0.19	~ 0	0.17	~ 0	0.17	0.25	0.24	~ 0	0.20	~ 0	0.26
90	~ 0	0.09	~ 0	0.38	~ 0	0.18	~ 0	0.23	~ 0	0.41	~ 0	0.71
100	~ 0	0.18	~ 0	0.22	~ 0	0.24	~ 0	0.13	~ 0	0.25	~ 0	0.25
130	~ 0	0.22	~ 0	0.11	~ 0	0.25	~ 0	0.22	~ 0	0.23	~ 0	0.11
140	~ 0	0.23	0.10	0.07	~ 0	0.28	~ 0	0.30	~ 0	0.26	~ 0	0.58
150	~ 0	0.24	~ 0	0.06	~ 0	0.24	0.20	0.06	~ 0	0.27	~ 0	0.45
160	~ 0	0.24	~ 0	0.04	~ 0	0.25	-0.20	0.15	~ 0	0.31	~ 0	0.20

Table 10. Experimental results and total uncertainties (δ) for estimation of direct stiffness and effective damping (Figure 12).

Inlet LVF = 3%

	Pocket Damper Seal											
	Ω = 0 rpm				**Ω = 3000 rpm**				**Ω = 5250 rpm**			
ω	**K [MN/m]**	**δK_{total} [MN/m]**	**C_{eff} [kN-s/m]**	**$\delta C_{eff,total}$ [kN-s/m]**	**K [MN/m]**	**δK_{total} [MN/m]**	**C_{eff} [kN-s/m]**	**$\delta C_{eff,total}$ [kN-s/m]**	**K [MN/m]**	**δK_{total} [MN/m]**	**C_{eff} [kN-s/m]**	**$\delta C_{eff,total}$ [kN-s/m]**
10	-0.91	0.57	~ 0	1.79	~ 0	0.88	-9.65	2.31	~ 0	1.12	-11.98	3.14
20	-0.81	0.43	4.59	1.17	~ 0	1.48	-6.45	3.96	~ 0	0.66	-9.95	1.97
30	~ 0	0.50	2.99	1.04	-0.50	0.31	-2.62	1.64	-0.77	0.34	-1.95	0.28
70	0.56	0.38	2.54	0.89	-0.64	0.53	2.29	1.37	-0.93	0.60	2.15	0.89
90	~ 0	0.12	0.51	0.50	~ 0	0.57	1.79	0.71	~ 0	1.17	~ 0	2.31
100	~ 0	0.21	0.82	0.32	~ 0	0.33	1.16	0.34	-0.26	0.20	1.29	1.05
130	0.57	0.21	0.74	0.26	~ 0	0.22	0.85	0.20	~ 0	0.32	~ 0	0.54
140	0.67	0.25	0.37	0.28	0.26	0.23	0.77	0.63	~ 0	0.41	1.03	0.71
150	0.40	0.25	~ 0	0.26	~ 0	0.32	0.85	0.75	~ 0	0.49	0.90	0.31
160	0.35	0.25	0.20	0.13	~ 0	0.24	0.48	0.46	~ 0	0.38	0.62	0.58
	Labyrinth Seal											
	Ω = 0 rpm				**Ω = 3000 rpm**				**Ω = 5250 rpm**			
ω	**K [MN/m]**	**δK_{total} [MN/m]**	**C_{eff} [kN-s/m]**	**$\delta C_{eff,total}$ [kN-s/m]**	**K [MN/m]**	**δK_{total} [MN/m]]**	**C_{eff} [kN-s/m]**	**$\delta C_{eff,total}$ [kN-s/m]**	**K [MN/m]**	**δK_{total} [MN/m]**	**C_{eff} [kN-s/m]**	**$\delta C_{eff,total}$ [kN-s/m]**
10	~ 0	0.22	-0.18	0.15	~ 0	0.25	-1.26	0.19	~ 0	~ 0	0.47	0.17
20	~ 0	0.22	0.24	0.08	~ 0	0.26	~ 0	0.19	~ 0	~ 0	0.30	0.10
30	~ 0	0.22	~ 0	0.13	~ 0	0.28	~ 0	0.20	~ 0	~ 0	0.58	0.11
70	~ 0	0.19	~ 0	0.21	~ 0	0.19	0.49	0.34	~ 0	0.20	~ 0	0.34
90	~ 0	0.10	~ 0	0.39	~ 0	0.22	0.32	0.24	~ 0	~ 0	0.58	0.46
100	~ 0	0.18	~ 0	0.23	~ 0	0.22	~ 0	0.28	~ 0	0.24	~ 0	0.43
130	~ 0	0.22	0.25	0.12	~ 0	0.24	0.30	0.26	~ 0	0.24	~ 0	0.28
140	~ 0	0.23	0.20	0.07	~ 0	0.25	~ 0	0.24	~ 0	0.27	~ 0	0.25
150	~ 0	0.24	~ 0	0.09	~ 0	0.28	0.45	0.23	~ 0	0.24	~ 0	0.29
160	~ 0	0.24	~ 0	0.07	~ 0	0.31	~ 0	0.48	~ 0	0.30	~ 0	0.68

Table 11. Experimental results and total uncertainties (δ) for estimation of direct stiffness and effective damping (Figure 13).

Inlet LVF = 5%

	Pocket Damper Seal											
	Ω = 0 rpm				**Ω = 3000 rpm**				**Ω = 5250 rpm**			
ω	**K [MN/m]**	**δK_{total} [MN/m]**	**C_{eff} [kN-s/m]**	**$\delta C_{eff,total}$ [kN-s/m]**	**K [MN/m]**	**δK_{total} [MN/m]**	**C_{eff} [kN-s/m]**	**$\delta C_{eff,total}$ [kN-s/m]**	**K [MN/m]**	**δK_{total} [MN/m]**	**C_{eff} [kN-s/m]**	**$\delta C_{eff,total}$ [kN-s/m]**
10	-1.10	0.37	2.37	2.15	~ 0	1.26	-7.79	2.54	~ 0	1.08	-3.32	3.14
20	-0.67	0.62	5.29	0.75	~ 0	1.46	-8.06	1.66	~ 0	0.26	-5.71	0.70
30	~ 0	0.53	5.04	1.19	-0.32	0.23	-5.53	0.38	-0.38	0.32	-4.30	0.41
70	0.44	0.19	1.93	0.74	~ 0	0.64	1.05	0.45	~ 0	0.54	1.32	0.43
90	0.40	0.27	1.56	0.87	~ 0	0.25	0.95	0.51	~ 0	0.70	~ 0	1.92
100	0.55	0.12	~ 0	0.43	0.27	0.19	0.61	0.41	~ 0	0.43	0.93	0.62
130	~ 0	0.21	~ 0	0.26	~ 0	0.28	0.56	0.21	~ 0	0.25	~ 0	0.71
140	~ 0	0.22	0.39	0.13	~ 0	0.31	~ 0	0.51	0.36	0.30	~ 0	1.05
150	~ 0	0.23	0.40	0.16	0.34	0.24	0.64	0.34	0.33	0.25	~ 0	0.72
160	~ 0	0.24	0.52	0.32	0.40	0.24	~ 0	0.66	~ 0	0.35	~ 0	0.72
	Labyrinth Seal											
	Ω = 0 rpm				**Ω = 3000 rpm**				**Ω = 5250 rpm**			
ω	**K [MN/m]**	**δK_{total} [MN/m]**	**C_{eff} [kN-s/m]**	**$\delta C_{eff,total}$ [kN-s/m]**	**K [MN/m]**	**δK_{total} [MN/m]]**	**C_{eff} [kN-s/m]**	**$\delta C_{eff,total}$ [kN-s/m]**	**K [MN/m]**	**δK_{total} [MN/m]**	**C_{eff} [kN-s/m]**	**$\delta C_{eff,total}$ [kN-s/m]**
10	~ 0	0.23	0.32	0.13	~ 0	0.27	1.71	0.56	~ 0	0.26	3.37	0.19
20	~ 0	0.22	~ 0	0.09	~ 0	0.23	~ 0	0.77	~ 0	0.21	~ 0	0.29
30	~ 0	0.22	0.44	0.13	~ 0	0.27	~ 0	0.34	~ 0	0.24	~ 0	0.38
70	~ 0	0.22	~ 0	0.22	~ 0	0.17	~ 0	0.26	~ 0	0.20	~ 0	0.43
90	~ 0	0.07	0.44	0.40	~ 0	0.19	0.70	0.54	~ 0	0.23	~ 0	0.63
100	~ 0	0.18	~ 0	0.25	~ 0	0.22	~ 0	0.32	~ 0	0.22	0.25	0.17
130	~ 0	0.21	0.34	0.15	~ 0	0.24	0.50	0.18	~ 0	0.26	0.27	0.26
140	~ 0	0.23	0.27	0.15	~ 0	0.24	~ 0	0.48	~ 0	0.23	~ 0	0.25
150	~ 0	0.23	0.26	0.12	~ 0	0.24	0.46	0.23	~ 0	0.26	~ 0	0.38
160	~ 0	0.24	0.08	0.06	~ 0	0.25	~ 0	0.27	~ 0	0.33	~ 0	0.69